

Long-term GRMHD Simulations of Neutron Star Merger Accretion Disks: Implications for Electromagnetic Counterparts

Rodrigo Fernández^{1*}, Alexander Tchekhovskoy², Eliot Quataert^{3,4}, Francois Foucart⁵, and Daniel Kasen^{3,4,6}

¹ *Department of Physics, University of Alberta, Edmonton, AB T6G 2E1, Canada*

² *Center for Interdisciplinary Exploration & Research in Astrophysics (CIERA), Physics & Astronomy, Northwestern University, Evanston, IL 60202, USA*

³ *Department of Astronomy & Theoretical Astrophysics Center, University of California, Berkeley, CA 94720, USA*

⁴ *Department of Physics, University of California, Berkeley, CA 94720, USA*

⁵ *Department of Physics and Astronomy, University of New Hampshire, Durham, NH 03824, USA*

⁶ *Nuclear Science Division, Lawrence Berkeley National Laboratory, Berkeley, CA 94720, USA*

Submitted to MNRAS

ABSTRACT

We investigate the long-term evolution of black hole accretion disks formed in neutron star mergers. These disks expel matter that contributes to an r -process kilonova, and can produce relativistic jets powering short gamma-ray bursts. Here we report the results of a three-dimensional, general-relativistic magnetohydrodynamic (GRMHD) simulation of such a disk which is evolved for long enough (~ 9 s, or $\sim 6 \times 10^5 r_g/c$) to achieve completion of mass ejection far from the disk. Our model starts with a poloidal field, and fully resolves the most unstable mode of the magnetorotational instability. We parameterize the dominant microphysics and neutrino cooling effects, and compare with axisymmetric hydrodynamic models with shear viscosity. The GRMHD model ejects mass in two ways: a prompt MHD-mediated outflow and a late-time, thermally-driven wind once the disk becomes advective. The total amount of unbound mass ejected ($0.013 M_\odot$, or $\approx 40\%$ of the initial torus mass) is twice as much as in hydrodynamic models, with higher average velocity ($0.1c$) and a broad electron fraction distribution with a lower average value (0.16). Scaling the ejected fractions to a disk mass of $\sim 0.1 M_\odot$ can account for the red kilonova from GW170817 but underpredicts the blue component. About $\sim 10^{-3} M_\odot$ of material should undergo neutron freezeout and could produce a bright kilonova precursor in the first few hours after the merger. With our idealized initial magnetic field configuration, we obtain a robust jet and sufficient ejecta with Lorentz factor $\sim 1 - 10$ to (over)produce the non-thermal emission from GW170817.

Key words: accretion, accretion disks — gravitation — MHD — neutrinos — nuclear reactions, nucleosynthesis, abundances – stars: black holes

1 INTRODUCTION

The recent detection of the neutron star (NS) merger GW170817¹ in gravitational- and electromagnetic waves (Abbott et al. 2017c,d, and references therein) has advanced several outstanding issues in astrophysics. It has established neutron star mergers as an important (if not dominant) site of r -process element production (e.g., Kasen et al. 2017; Côté et al. 2018; Hotokezaka et al. 2018), provided unambiguous association between a neutron star merger and a short gamma-ray burst (Abbott et al. 2017b), and set constraints on the dense-matter equation of state (e.g., Bauswein et al. 2017; Margalit

& Metzger 2017; Rezzolla et al. 2018; Chatziioannou et al. 2018; Raihel et al. 2018; De et al. 2018; Abbott et al. 2018).

Evidence for the r -process comes from the photometric and spectroscopic properties of the observed kilonova (e.g., Cowperthwaite et al. 2017; Chornock et al. 2017; Drout et al. 2017; Tanaka et al. 2017; Tanvir et al. 2017). This type of transient had been predicted to arise out of sub-relativistic, neutron-rich ejecta from the merger that is radioactively heated by freshly produced r -process elements (Li & Paczyński 1998; Metzger et al. 2010; Roberts et al. 2011; Tanaka 2016; Metzger 2017). The optical opacity of lanthanides and actinides ($A > 130$, produced by the r -process) is such that the transient was expected to evolve from blue optical to near infrared within a few days (Kasen et al. 2013; Tanaka & Hotokezaka 2013; Barnes & Kasen 2013; Fontes et al. 2015), as observed. Also, the temporal evolution of the bolometric luminosity

* E-mail: rafernan@ualberta.ca

¹ Also known as GRB170817A, SSS17a, AT 2017gfo, and DLT17ck

is consistent with the time-dependence of the radioactive heating rate from the r -process (e.g., Rosswog et al. 2017).

Two main mass ejection channels operate in neutron star mergers: dynamical ejecta and outflows from the remnant accretion disk. The former is launched on the dynamical time of the merger (\sim ms) by tidal forces and hydrodynamic interactions (e.g., Bauswein et al. 2013; Hotokezaka et al. 2013). Numerical relativity simulations predict this material to be sufficiently neutron-rich to produce mainly $A > 130$ elements, with varying amounts of lighter material depending on the equation of state (EOS) of dense matter and the treatment of neutrino physics (e.g., Wanajo et al. 2014; Roberts et al. 2017; Radice et al. 2016; Foucart et al. 2016,?). While magnetic fields are not expected to significantly alter the dynamics of the merger (e.g., Endrizzi et al. 2016) they can lead to some mass ejection on the dynamical time (e.g., Kiuchi et al. 2014; Shibata et al. 2017). For the particular case of GW710817, the amount of dynamical ejecta expected is smaller than the total r -process mass inferred from the kilonova (e.g., Abbott et al. 2017a; Shibata et al. 2017; however see Kawaguchi et al. 2018 for a different kilonova mass estimate).

The remnant accretion disk evolves on longer timescales (\sim 100 ms - 10 s) and ejects mass through a combination of physical processes (see, e.g., Fernández & Metzger 2016 for an overview). Immediately after the merger, the disk is sufficiently hot and dense for neutrinos to be the primary cooling channel, with most of the nuclei fully dissociated into nucleons (Popham et al. 1999; Ruffert & Janka 1999; Narayan et al. 2001; Chen & Beloborodov 2007). A key property of these disks is that they transition to being fully advective once the density drops and weak interactions freeze-out on a timescale of \sim 300 ms to 1 s, making them prone to launching outflows (Metzger et al. 2009).

Our current understanding of the long-term disk evolution is based primarily on axisymmetric hydrodynamic simulations that include the required microphysics and neutrino treatment at various levels of sophistication, but which model angular momentum transport through an imposed shear stress with parameterized viscosity (e.g., Fernández & Metzger 2013a; Just et al. 2015; Fujibayashi et al. 2018). With this physics included, the outflow is driven primarily by viscous heating and nuclear recombination, with neutrino heating being sub-dominant when the central object is a black hole (BH). The amount of mass ejected in these simulations lies in the range \sim 5 – 20% of the initial disk mass after an evolution time of \sim 10 s, with quantitative details depending primarily on the properties of the central object (a much larger fraction of the disk can be ejected if a hypermassive neutron star forms; Metzger & Fernández 2014). The composition of the outflow involves mainly light r -process elements, with varying amounts of material with $A > 130$ depending on parameters such as the strength of angular momentum transport or the lifetime of a hypermassive neutron star (HMNS) (Just et al. 2015; Martin et al. 2015; Wu et al. 2016; Lippuner et al. 2017).

It is generally accepted, however, that angular momentum transport in astrophysical accretion disks operates via magneto-hydrodynamic (MHD) turbulence driven by the magnetorotational instability (MRI; Balbus & Hawley 1991). Early GRMHD models of NS-NS/BH-NS merger remnant disks employed axisymmetric (2D) simulations that start with an initially poloidal field geometry, and which include the relevant neutrino processes, but (1) had too high an ambient density to allow for a significant outflow and/or (2) did not evolve the system for long enough to achieve the radiatively-inefficient state and completion of mass ejection (Shibata et al. 2007; Shibata & Sekiguchi 2012; Janiuk et al. 2013;

Janiuk 2017). In addition, it is well-known that in axisymmetry, as a consequence of the anti-dynamo theorem (Cowling 1933), MRI turbulence dissipates within \sim 10 disk orbits (e.g. Hawley 2000) and hence angular momentum transport cannot be sustained for the required timescales.

Recently, Siegel & Metzger (2017, 2018) have reported the first three-dimensional (3D) GRMHD simulation of an accretion disk around a black hole remnant. The simulation uses a physical equation of state that includes recombination of nucleons into alpha particles, and accounts for neutrino cooling via a leakage scheme. They start their simulation with an equilibrium torus and an initial poloidal field, evolving the disk for \sim 400 ms. Strong outflows are obtained, and by the end of their simulation 20% of the initial disk mass is ejected as unbound matter at a radius of 10^8 cm, with 60% of the disk mass accreted. Since by that time accretion onto the BH is mostly complete, they surmise that the remaining 20% would continue to be ejected as an unbound outflow if the simulation was continued to longer times. Nouri et al. (2017) also studied the GRMHD evolution of an accretion disk mapped from a 3D non-magnetized numerical relativity simulation of a BH-NS merger, endowing the disk with a poloidal field and following its evolution for 60 ms, reaching a fully developed MRI and comparing with the non-magnetized case.

While there is an existing body of work on the long-term evolution of black hole accretion disks, including a number of 3D GRMHD studies (e.g., McKinney et al. 2012), work has focused primarily on systems arising in X-ray binaries and active galactic nuclei, for which thermodynamic conditions, disk size, and the effect of photons and neutrinos are very different than for NS-NS/NS-BH mergers. Because of these differences, the results of previous work that focused on the sub-relativistic disk outflow (e.g., Narayan et al. 2012; Sądowski et al. 2013) are not directly applicable to the merger problem.

In this paper we close the gap in disk evolution time by performing long-term GRMHD simulations of NS merger accretion disks that for the first time achieve completion of mass ejection (i.e., most of the initial disk material either accreted or ejected). In order to minimize the computational cost and evolve our simulations for as long as possible, we employ a number of approximations to the microphysics and neutrino treatment. We focus on understanding the basic properties of the sub-relativistic outflow when MHD turbulence transports angular momentum. To carry out our simulations, we extend the GRMHD code `HARMPT`² to include the dominant microphysics and neutrino source terms. Simulations are evolved for long enough (several times $10^5 r_g/c$, with $r_g = GM_{\text{bh}}/c^2$ the gravitational radius of a black hole of mass M_{bh}) to achieve the advective state in the disk evolution and to reach completion of mass ejection. While our models resolve the MRI, we consider our work to be exploratory in nature, because not only more spatial resolution but also more physics and realistic initial conditions are required to make quantitative predictions on the wind contribution to the kilonova and r -process nucleosynthesis, particularly due to the sensitivity of the latter to the exact outflow composition.

Given that until now only hydrodynamic disk models have been evolved into the advective state, and that a key mass ejection mechanism (thermal energy deposition by angular momentum transport and nuclear recombination) is present in both approaches, we compare the results of our GRMHD simulation with those from hydrodynamic models that employ an alpha viscosity to transport

² Available at <https://github.com/atckehko/harmpt>

angular momentum. The goal is to identify similarities and differences in mass ejection, thus providing a solid foundation to understand the behavior of the GRMHD model.

The structure of the paper is the following. Section 2 describes our computational setup, §3 presents our results, §4 discusses the observational implications, and §5 closes with a summary and future prospects. The Appendix presents a detailed description of the microphysics included, and a comparison with more complete hydrodynamic models.

2 COMPUTATIONAL METHODOLOGY

2.1 Physical Model

Our goal is to study the long-term evolution of the accretion disk that forms during the dynamical phase of a NS-NS or a BH-NS merger, assuming that the central remnant is a promptly-formed BH. This requires the mass of the remnant to exceed a certain threshold that depends on the dense matter EOS (e.g., Shibata & Taniguchi 2006). Since the spacetime around the BH settles into a stationary configuration a few light crossing times after the end of the merger (e.g., Lehner & Pretorius 2014), we adopt a static Kerr metric. We adopt a black hole mass $M_{\text{bh}} = 3M_{\odot}$ with spin $a = 0.8$ (e.g., Kastaun et al. 2013; Bernuzzi et al. 2014) as a fiducial value for a generic NS-NS merger³. Disks formed in BH-NS mergers are expected to follow the same qualitative evolution as disks from NS-NS mergers, with quantitative differences due to the higher mass of the central BH.

In order to maximize the physical time evolved in our simulation given fixed computational resources and HARMPI capabilities, we employ an EOS with constant adiabatic index γ_{ad} in all of our calculations. We choose the value of γ_{ad} by comparing the results of 2D hydrodynamic wind models that use a physical EOS (Fernández et al. 2015, hereafter F15) with those obtained using an ideal gas (§2.3). The results of this comparison are presented in Appendix A. Good agreement in the wind properties is obtained when using $\gamma_{\text{ad}} = 4/3$, which is consistent with the dominance of radiation pressure at large radii. Minor quantitative differences are obtained in the inner regions of the disk, where the pressure at early times is dominated by an ideal gas of non-relativistic ions, and where electrons are relativistic and mildly degenerate.

The temperature of the gas is obtained by assuming that the total pressure P has contributions from radiation and an ideal gas of neutrons, protons, and electrons

$$P = P_{\text{gas}} + P_{\text{rad}} \quad (1)$$

$$P = [1 + Y_e] \frac{\rho k T}{m_n} + \frac{1}{3} a_{\text{rad}} T^4, \quad (2)$$

where ρ , T , and Y_e are the gas density, temperature, and electron fraction, a_{rad} is the radiation constant, and we have neglected the mass difference between neutrons and protons. In the densest parts of the disk, at early times, the pressure is dominated by nucleons, so the assumption of non-degeneracy for the electron pressure contribution is not important. As shown in §A1, at late times the wind is dominated by radiation pressure, thus the assumption of non-degeneracy of electrons in equation (2) is also secondary. Electron

degeneracy is nevertheless included in the calculation of the neutrino source terms below. Equation (2) yields the temperature given the pressure, density, and electron fraction.

We account for the emission of electron neutrinos and antineutrinos through charged-current weak interactions on nucleons. Neutrino absorption is ignored, which is a reasonable first approximation when a black hole forms promptly (e.g., Just et al. 2015). We employ the approximate emission rates of Janka (2001), which are valid for temperatures $kT \gg (m_n - m_p)c^2 \simeq 1.3$ MeV. At lower temperatures, neutrino emission is unimportant, so this approximation captures the dominant effect. Neutrino and antineutrino emission causes the electron fraction and internal energy to change in the local fluid frame at rates that are, respectively,

$$\Gamma = \frac{4c(1 + g_A^2)}{(hc)^3} \mathcal{F}_4(0) \left[\frac{G_{\text{F}}}{(\hbar c)^2} \right]^2 (kT)^5 D_4(\eta_e, X_n, X_p) \approx 0.22 T_{10}^5 D_4(\eta_e, X_n, X_p) \quad [\text{s}^{-1}] \quad (3)$$

$$Q = -\frac{4c(1 + g_A^2)}{m_n(hc)^3} \mathcal{F}_5(0) \left[\frac{G_{\text{F}}}{(\hbar c)^2} \right]^2 (kT)^6 D_5(\eta_e, X_n, X_p) \approx -8.9 \times 10^{17} T_{10}^6 D_5(\eta_e, X_n, X_p) \quad [\text{erg g}^{-1} \text{s}^{-1}], \quad (4)$$

where X_n and X_p are the mass fractions of neutrons and protons, respectively, and the degeneracy parameter is $\eta_e = \mu_e/(kT)$, with μ_e the electron chemical potential (Appendix A). Other physical constants have their standard meanings. Suppression of emission in neutrino-opaque regions is approximated by multiplying Γ and Q by $e^{-\tau_\nu}$, with

$$\tau_\nu = \rho/10^{11} \text{ g cm}^{-3} \quad (5)$$

an approximation to the neutrino optical depth to charged-current weak interactions. This approximation is acceptable as long as the optical depth in the disk is small (see §2.4 for details on the initial torus properties).

The effects of degeneracy and composition enter into the neutrino source terms (equations 3-4) through the dimensionless functions

$$D_4(\eta_e, X_n, X_p) = [X_n \mathcal{F}_4(-\eta_e) - X_p \mathcal{F}_4(\eta_e)] / \mathcal{F}_4(0) \quad (6)$$

$$D_5(\eta_e, X_n, X_p) = [X_n \mathcal{F}_5(-\eta_e) + X_p \mathcal{F}_5(\eta_e)] / \mathcal{F}_5(0), \quad (7)$$

where

$$\mathcal{F}_j(\eta) = \int_0^\infty \frac{x^j dx}{e^{x-\eta} + 1}. \quad (8)$$

are the Fermi functions. Analytical approximations are adopted for these integrals, with details provided in Appendix A.

The equilibrium electron fraction implied by equation (3), including only neutrons and protons, is given by the condition $D_4(\eta_e, 1 - Y_e^{\text{eq}}, Y_e^{\text{eq}}) = 0$, or

$$Y_e^{\text{eq}} = \frac{\mathcal{F}_4(-\eta_e)}{\mathcal{F}_4(\eta_e) + \mathcal{F}_4(-\eta_e)} \simeq \begin{cases} \frac{1}{2(1 + \eta_e)} & \eta_e \ll 1 \\ \frac{5!}{\eta_e^5} e^{-\eta_e} & \eta_e \gg 1. \end{cases} \quad (9)$$

We include the contribution of the nuclear binding energy of α particles to the internal energy through a source term

$$\Delta q_{\text{nuc}} = \frac{B_\alpha}{m_\alpha} \Delta X_\alpha \quad (10)$$

$$= 6.8 \times 10^{18} \Delta X_\alpha \text{ erg g}^{-1}, \quad (11)$$

where $B_\alpha = 28.3$ MeV and m_α are the nuclear binding energy and mass of an α particle, respectively, and ΔX_α is the change in the

³ At the time our parameters were chosen and our runs were completed, GW170817 had not yet been detected.

mass fraction of alpha particles (X_α). The source term is applied implicitly at each time step in the fluid rest frame,

$$e_{\text{int}}^{n+1} - \frac{B_\alpha}{m_\alpha} X_\alpha^{n+1} = e_{\text{int}}^n - \frac{B_\alpha}{m_\alpha} X_\alpha^n + Q^n \Delta t, \quad (12)$$

where e_{int} is the specific internal energy, Δt is the simulation time step, and the time discretization is labeled by the superscript n (an additional factor of $(u^t)^{-1}$ is added to Q in GRMHD, c.f. equation 21). With this notation, $\Delta X_\alpha = X_\alpha^{n+1} - X_\alpha^n$. Equation (12) is applied after Y_e has been updated with the neutrino source term in equation (3), hence ρ and Y_e are kept constant in the iteration (a simultaneous update of the temperature via equation [2] is also required). The mass fraction X_α is computed using the analytic fit to Nuclear Statistical Equilibrium (NSE) of Woosley & Baron (1992)⁴

$$X_\alpha = \min[2Y_e, 2(1 - Y_e)](1 - \min[1, X_{\text{WB}}]) \quad (13)$$

$$X_{\text{WB}} = 15.58 \frac{T^{9/8}}{\rho_{10}^{3/4}} \exp(-7.074/T_{\text{MeV}}), \quad (14)$$

where X_{WB} is the sum of the mass fractions of neutrons and protons available to make α particles. The numerical prefactor in equation (14) has been adjusted slightly to improve agreement in the density regime of interest (Appendix A). The mass fractions of neutrons and protons are obtained for every new value of X_α , given Y_e , from conservation of baryon number and charge,

$$X_n + X_p + X_\alpha = 1 \quad (15)$$

$$X_p + \frac{1}{2}X_\alpha = Y_e. \quad (16)$$

2.2 GRMHD Simulations in 3D

To evolve the torus in GRMHD, we use HARMPT², an enhanced version of the serial open-source code HARM (Gammie et al. 2003; Noble et al. 2006). Updates include extension to three spatial dimensions and parallelization with the Message Passing Interface (Tchekhovskoy et al., in preparation). The code has also been extended to include the physics described in §2.1. Specifically, we solve the ideal GRMHD equations on a Kerr metric, with energy source terms due to neutrinos and nuclear recombination, and supplemented by a lepton number conservation equation for the evolution of Y_e :

$$(-g)^{-1/2} \partial_\mu (\sqrt{-g} \rho u^\mu) = 0 \quad (17)$$

$$\partial_\mu (\sqrt{-g} T^\mu_\nu) = \sqrt{-g} T^\lambda_k \Gamma^\lambda_{\nu k} \quad (18)$$

$$\partial_t (\sqrt{-g} B^i) = -\partial_j [\sqrt{-g} (b^j u^i - b^i u^j)] \quad (19)$$

$$(-g)^{-1/2} \partial_\mu (\sqrt{-g} \rho \mathbf{X} u^\mu) = 0. \quad (20)$$

where $g = \det(g_{\mu\nu})$ is the determinant of the Kerr metric, ρ is the rest mass density, \mathbf{X} is a composition vector that includes Y_e and other mass fractions, and $c = 1$ has been assumed. As conventional, greek indices run in the range $\{0-4\}$ while latin indices over $\{1-3\}$, with lower and upper indices denoting covariant and contravariant components, respectively. The energy and lepton number source terms are applied in the local fluid rest frame in between updates of

⁴ The fit of Woosley & Baron (1992) was derived in the context of accretion-induced collapse of white dwarfs to neutron stars, for which $Y_e \approx 0.5$. For neutron-rich material, a fraction $(1 - 2Y_e)$ of the neutrons is not available to form α particles.

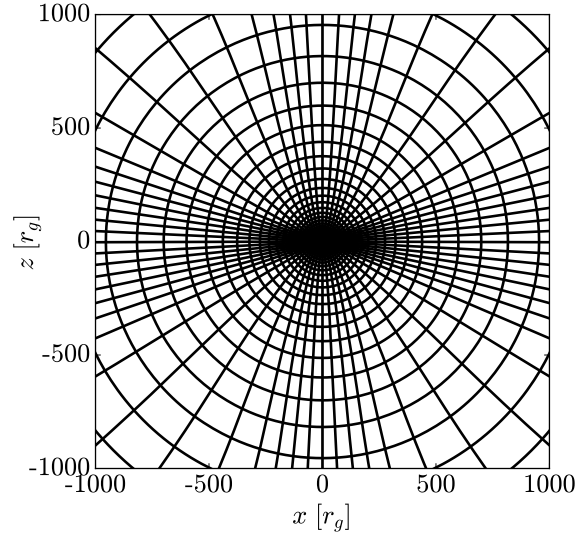


Figure 1. Meridional slice through the numerical grid used for our GRMHD simulation. The grid focuses the resolution on both the polar regions, where the relativistic jets form, and the equatorial plane, where the turbulent accretion disk resides. This allows us to obtain accurate descriptions of both the accretion disk, jets and outflows. For clarity, we show every 8th grid line.

conserved quantities,

$$\Delta \epsilon = \rho \left(Q \frac{\Delta t}{u^t} + \Delta q_{\text{nuc}} \right) \quad (21)$$

$$\Delta(\rho Y_e) = \rho \Gamma \frac{\Delta t}{u^t}. \quad (22)$$

where $\epsilon = \rho e_{\text{int}} = P/(\gamma_{\text{ad}} - 1)$ is the internal energy density, and equation (21) is solved implicitly at each time step (equation 12). In this unit system, Q and q_{nuc} must be divided by c^3/r_g , and Γ by c/r_g . The magnetic field 4-vector is denoted by b^μ , and the magnetic field 3-vector is B^i . The stress-energy tensor is

$$T^{\mu\nu} = (\rho + \epsilon + P + b_\lambda b^\lambda) u^\mu u^\nu + \left(P + \frac{1}{2} b_\lambda b^\lambda \right) g^{\mu\nu} - b^\mu b^\nu. \quad (23)$$

With this notation, a factor of $(4\pi)^{-1/2}$ has been absorbed in the definition of b .

The code solves equations (17)-(20) in conservation form. Mapping from conserved to primitive variables is carried out with the two-dimensional algorithm of Noble et al. (2006). Fluxes of conserved quantities are computed with a local Lax-Friedrichs method using linear reconstruction and a monotized central slope limiter. Enforcement of $\nabla \cdot \mathbf{B} = 0$ is achieved with the constrained transport method of Tóth (2000) that uses a cell-centered representation of the magnetic field.

The computational grid is discretized in spherical-polar-like modified Kerr-Schild coordinates. We distribute the radial grid of 512 cells as follows. The first 458 cells are logarithmically spaced between the inner radius $r_{\text{min}} = 0.87r_h = 1.392r_g$ and the transition radius $r_{\text{tr}} = 10^4 r_g$, yielding $\Delta r/r \approx 0.02$. Here, $r_h = (1 + \sqrt{1 - a^2})r_g = 1.6r_g$ is the event horizon radius. Thus, our inner radial boundary resides 7 cells inside of the event horizon, thereby ensuring that no signals reach from the boundary to outside of the event horizon, as is physically required. To avoid the interaction between the expanding accretion disk and the outer boundary, we extend the grid out to $r_{\text{max}} = 10^5 r_g$: at $r > r_{\text{tr}}$, the radial grid be-

comes progressively sparse, with the remaining 54 cells resolving the distance between r_{tr} and r_{max} . The meridional grid of 256 cells covers the range $[0, \pi]$, and is “cylindrified” close to the polar axis to save computational time, as in Tchekhovskoy et al. (2011). Figure 1 shows that the meridional grid focuses the resolution both in the polar regions, to resolve the magnetized collimated relativistic jets, and in the equatorial plane, to resolve the turbulent accretion disk. This focusing approximately doubles the effective resolution in the equatorial disk region, increasing it to ≈ 510 cells, and increases the resolution by a factor of ≈ 1.5 in the polar regions, to ≈ 370 cells, at large radii ($r \gtrsim 10^3 r_g$). The azimuthal grid is uniform, covering the range $[0, \pi]$ (half of the disk) with 64 cells. The boundary conditions are outflow in the radial direction, reflective in the meridional direction, and periodic in the azimuthal direction.

2.3 Axisymmetric Hydrodynamic Simulations with shear viscosity

To compare with previous work, and to help diagnose the GRMHD simulation, we also carry out 2D hydrodynamic simulations that transport angular momentum with a shear viscosity following the parameterization of Shakura & Sunyaev (1973). The models are carried out in a modified version of FLASH3 (Fryxell et al. 2000; Dubey et al. 2009) that has been equipped with the physics required to simulate merger remnant accretion disks (Fernández & Metzger 2013a,b; Metzger & Fernández 2014; F15).

The code solves the equations of mass, poloidal momentum, angular momentum, energy, and lepton number conservation in spherical polar coordinates (r, θ) with source terms due to gravity, shear viscosity, and neutrinos,

$$\frac{\partial \rho}{\partial t} + \nabla \cdot (\rho \mathbf{v}_p) = 0 \quad (24)$$

$$\frac{d\mathbf{v}_p}{dt} = -\frac{1}{\rho} \nabla P - \nabla \Phi_A \quad (25)$$

$$\rho \frac{d\ell_z}{dt} = r \sin \theta (\nabla \cdot \mathbb{T})_\phi \quad (26)$$

$$\rho \frac{de_{\text{int}}}{dt} + p \nabla \cdot \mathbf{v}_p = \frac{1}{\rho v} \mathbb{T} : \mathbb{T} + \rho \left(Q + \frac{B_\alpha}{m_\alpha} \dot{X}_\alpha \right) \quad (27)$$

$$\frac{dY_e}{dt} = \Gamma, \quad (28)$$

where $d/dt \equiv \partial/\partial t + \mathbf{v}_p \cdot \nabla$, \mathbf{v}_p is the poloidal velocity, $\ell_z = r \sin \theta v_\phi$ is the specific angular momentum along z . An explicit form of the shear stress tensor \mathbb{T} can be found in Fernández & Metzger (2013a). We only include the $r-\phi$ and $\theta-\phi$ components of the tensor so that the shear due to orbital motion is subject to viscous stresses but not poloidal motions such as thermally driven convection (following the approach of Stone et al. 1999).

The neutrino source terms and equation of state follow the approximations described in §2.1, while the gravity of the BH is modeled with the pseudo-Newtonian potential Φ_A of Artemova et al. (1996). An analytic form for this potential can be found in F15.

The computational grid covers the full range of polar angles $[0, \pi]$, with a radial range that extends from the average between the horizon and the ISCO radii on the inner side, $r_{\text{min}} = (r_h + r_{\text{ISCO}})/2 \approx 2.3 r_g$, until a radius 10^4 times larger. The spacing is logarithmic in radius and uniform in $\cos \theta$. The baseline resolution is 128 points per decade in radius and 112 points in the polar direction, yielding approximately square cells at the equator with $\Delta r/r \approx \Delta \theta \approx 0.018 \approx 1^\circ$. The boundary conditions are set to outflow at both radial ends, and reflecting in the θ -direction.

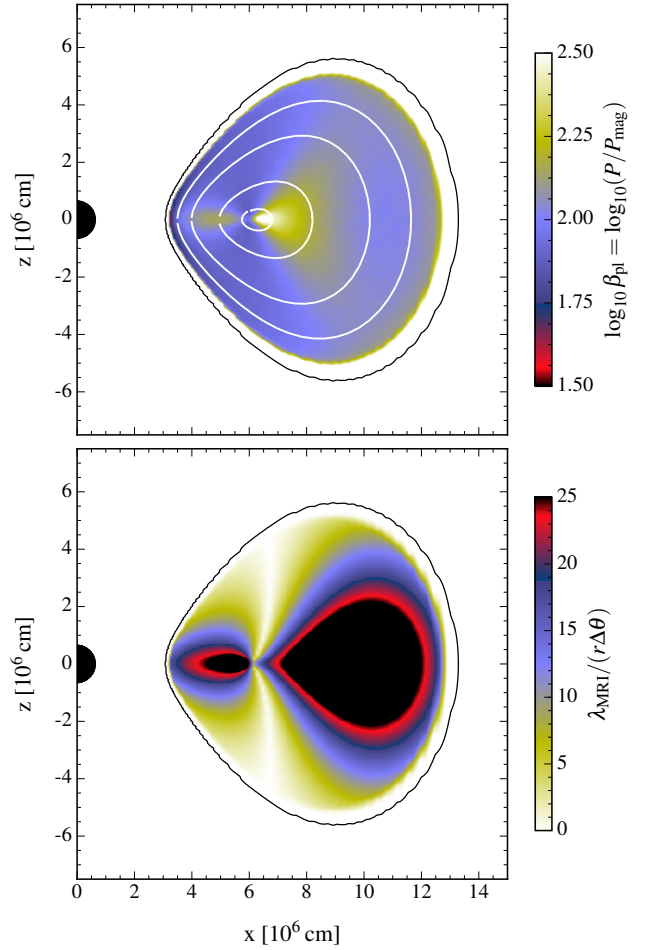


Figure 2. Initial condition for the GRMHD model. The black circle marks the inner boundary of the computational domain at $r_{\text{min}} = 1.4 r_g \approx 6.2 \times 10^5$ cm. **Top:** ratio β_{pl} of gas plus radiation pressure P (equation 2) to magnetic pressure P_{mag} (equation 29). The white contours show magnetic field lines, and the black contour shows the isodensity surface $\rho = 10^6 \text{ g cm}^{-3}$, close to the edge of the disk. The maximum field strength is approximately 4×10^{14} G. **Bottom:** Number of meridional cells that resolve the wavelength λ_{MRI} of the most unstable mode of the poloidal MRI. The black contour is the same as in the top panel.

2.4 Initial Conditions

The accretion disk is formed out of gravitationally bound material that has enough angular momentum to resist direct collapse to the BH. The material circularizes into a nearly axisymmetric configuration a few orbital times after the merger ($\lesssim 10$ ms, Ruffert & Janka 1999). Given that the evolutionary timescales that we are interested in are much longer than this circularization time, we take an equilibrium torus as the initial condition, and choose parameters to match representative merger systems. The results of Fernández et al. (2017) show that this approximation leads to qualitatively the same results in the late time viscously-driven outflow as when starting from the output of a dynamical merger calculation, with quantitative modifications to the electron fraction mass distribution of the order of $\sim 10\%$. More realistic initial conditions for the electron fraction are likely to affect material ejected promptly by magnetic fields (§3.1). Since this is the first long-term GRMHD simulation of a NS-NS merger remnant accretion disk, we focus on understanding the evolution of the system in isolation to identify intrinsic fea-

tures. A more realistic system would include an initial distribution of dynamical ejecta around the disk, which would modify the way in which both the jet and wind evolve (c.f., Fernández et al. 2017 for a BH-NS system; see also §3.6).

The initial equilibrium torus is constructed using a gravity consistent with each method: full Kerr metric for the GRMHD model (Fishbone & Moncrief 1976) or pseudo-Newtonian for hydrodynamic models (e.g., F15). The torus has an initial rest mass $M_{r0} = 0.033M_{\odot}$ in the GRMHD model and $0.030M_{\odot}$ in the hydrodynamic models, constant specific angular momentum and constant entropy $s = 8k_B$ per baryon, as well as constant initial electron fraction $Y_e = 0.1$. The radius of the density peak is chosen to be $r_0 = 50 \text{ km} \approx 11.3r_g$. The ratio of internal energy to gravitational energy at the density peak is 15%, resulting in $H/R \approx 0.35$ as generally obtained in full-physics simulations of NS-NS mergers (e.g., Sekiguchi et al. 2016). For the equilibrium torus solution in GR, this also corresponds to an inner radius of $0.62r_0$. The torus becomes optically-thin to neutrinos within the first few orbits, justifying the approximations described in §2.1.

A poloidal magnetic field is initially imposed in the GRMHD model following Tchekhovskoy et al. (2011). The magnetic vector potential satisfies $A \propto r^{5/(3(\gamma_{\text{ad}}-1))} \rho^2$, and is set to a constant when it drops below 10^{-3} of its maximum value, to prevent the magnetic field from reaching the low-density edge of the disk (Tchekhovskoy et al. 2011). Then, the magnetic field is renormalized at each point so it makes up a fixed fraction of matter plus radiation pressure. Next, a magnetic vector potential is computed by integrating up B^r and used for re-computing an updated magnetic field. This field is then normalized so that density-weighted ratio of matter and radiation pressure to magnetic pressure in the disk is $\langle \beta_{\text{pl}} \rangle = \langle P \rangle / \langle P_{\text{mag}} \rangle \approx 100$, where

$$P_{\text{mag}} = \frac{1}{2} b_{\mu} b^{\mu} \left[\frac{M_{\text{bh}} c^2}{r_g^3} \right]. \quad (29)$$

The advantage of recomputing the magnetic field as described above is in obtaining a more uniform distribution of β_{pl} in the disk; this is helpful for resolving the MRI. The resulting field configuration is shown in Figure 2. The maximum field strength is approximately $4 \times 10^{14} \text{ G}$. Given our spatial resolution, we resolve the most unstable wavelength of the poloidal MRI λ_{MRI} with at least 10 meridional cells ($r\Delta\theta$) over most of the equatorial plane, as also shown in Figure 2. Neutrino effects are not expected to modify the usual ideal MHD stability criterion in the torus (Foucart et al. 2015; Guilet et al. 2017).

The use of a finite volume method requires imposing a floor of density and internal energy. While a higher floor of density minimizes numerical problems near the inner radial boundary close to the BH, it also interferes with the launching of the wind if the mass in the outer computational domain becomes comparable to the mass ejected. We therefore adopt a floor of density that varies in both space and time. The floor ρ_f initially follows a power law with radius $\propto r^{-2}$, normalized so that $\rho_f = 10^{-5} \rho_{\text{max}}$ at $r = r_g$ (ρ_{max} is the initial maximum torus density). As the torus evolves, we decrease the density floor with time inside a transition radius $r_t = 4r_0 \approx 45r_g$ (following the approach of Just et al. 2015) to account for the fact that the disk density decreases with time. The functional form adopted is

$$\frac{\rho_f(r, t)}{\rho_t} = \begin{cases} \left[1 + \left(\frac{t}{t_v} + 1 \right)^{-2} \left(\left(\frac{r_t}{r} \right)^2 - 1 \right) \right] & r \leq r_t \\ \left(\frac{r_t}{r} \right)^2 & r > r_t, \end{cases} \quad (30)$$

where ρ_t is the initial density floor at $r = r_t$, and t_v is a characteristic timescale over which the density at the ISCO decreases, approximately 40 orbits at the density maximum for $\alpha = 0.03$. The time exponent comes from an empirical fit to the time dependence of the density at the inner boundary in F15. The floor of internal energy density in the GRMHD model is set to

$$\epsilon_f(r, t) = 10^{-7} \rho_{\text{max}} c^2 \left[\frac{\rho_f(r, t)}{\rho_f(r_g, t)} \right]_{\text{ad}}^{\gamma}. \quad (31)$$

Both floors are not allowed to decrease below $10^{-20} \rho_{\text{max}}$ (density) and $10^{-20} \rho_{\text{max}} c^2$ (internal energy density) in the GRMHD model. In the hydrodynamic models, a floor of specific internal energy p_f/ρ_f is used, with p_f chosen to be about 10^{-14} of the value at the initial pressure maximum.

At $t = 0$, the space surrounding the torus is filled with material with density $\approx 1.5\rho_f$, and a separate mass fraction $X_{\text{atm}} = 1$, modeling an inert hydrogen atmosphere ($Y_e = 1$). This mass fraction is included in the NSE system of equations (15)-(16) for continuity at the torus edges, but it is not available to form α particles (i.e., it is subtracted from the right hand side of equation 13).

Neutrino and nuclear source terms are set to zero when $\rho < 10\rho_f$. Given the difficulty of GRMHD schemes to recover primitive from conserved variables when the magnetic field dominates the energy density by large factors (e.g., Gammie et al. 2003), we ignore in our analysis any regions for which

$$\frac{b_{\mu} b^{\mu}}{\rho c^2} > 100. \quad (32)$$

Given that these highly magnetized regions (e.g., the center of the jet) are also associated with densities close to the floor value, we further ignore any part of the simulation for which $\rho < 10\rho_f$. In practice, these restrictions affect primarily the part of the outflow with the highest kinetic and electromagnetic energy, with very minor effects on the ejected mass distribution (§3.4.2).

2.5 Models Evolved

All production models are shown in Table 1. In addition to the GRMHD model B3d, we evolve three axisymmetric hydrodynamic models that differ only in the magnitude of the α viscosity parameter: h2d-v01 ($\alpha = 0.01$), h2d-v03 ($\alpha = 0.03$), and h2d-v10 ($\alpha = 0.1$). Aside from the initial magnetic field and viscosity parameters, all other properties in the initial tori are as close as possible between GRMHD and hydrodynamic models given the different implementations of gravity (the GRMHD torus has an initial rest mass $\sim 10\%$ higher than the hydrodynamic models).

3 RESULTS

3.1 Early disk evolution

The initial dynamics of the GRMHD model (B3d) is determined primarily by the choice of initial field geometry. Since the earliest stage of disk evolution leaves an imprint in the composition of the outflow, we discuss its properties keeping in mind that if more realistic initial conditions were used, it is unclear whether all of these features would be present.

The early evolution of the disk follows a sequence of stages involving mostly laminar flow (e.g., Hawley 2000). When starting with a purely poloidal field, orbital motion in the disk amplifies the toroidal magnetic field, and the resulting radial gradients in magnetic pressure drive the inner edge of the disk toward the black

Table 1. List of evolved models and summary of results. Columns from left to right show model name, dimensionality, viscosity parameter, evolution time in seconds and in $r_g/c = GM_{\text{bh}}/c^3 \approx 1.5 \times 10^{-5}$ s, unbound mass ejected at 10^9 cm in units of the initial torus mass ($M_{10} = 0.033M_{\odot}$ for GRMHD and $M_{10} = 0.030M_{\odot}$ for hydrodynamic models) and in M_{\odot} , average electron fraction and radial velocity of the outflow, unbound mass ejected that is lanthanide-poor ($Y_e > 0.25$) in units of the initial torus and in solar masses, and average velocity of lanthanide-poor outflow.

Model	dim.	α	t_{max}		M_{ej}		$\langle Y_e \rangle$	$\langle v^r/c \rangle$	$M_{\text{ej,LP}}$		$\langle v^r/c \rangle_{\text{LP}}$
			(s)	($10^5 r_g/c$)	(M_{10})	($10^{-3} M_{\odot}$)			(M_{10})	($10^{-3} M_{\odot}$)	
B3d	3D	...	9.3	6.3	0.39	13	0.16	11	0.04	1.2	22
h2d-v01	2D	0.01	26.5	18	0.16	4.8	0.26	2.7	0.06	1.9	3.1
h2d-v03	2D	0.03	16.5	11	0.21	6.3	0.20	3.2	0.04	1.1	4.5
h2d-v10	2D	0.10	8.8	5.9	0.22	6.7	0.17	5.2	0.03	0.8	10

hole, starting the accretion process. At the same time, the toroidal magnetic field changes sign on the disk equatorial plane, generating a current sheet and a vertical magnetic pressure gradient that compresses material.

Figure 3 illustrates this early evolution, which takes place within the first few orbits at the radius of the initial density peak (orbital period $t = 224 r_g/c \approx 3.3$ ms). Turbulence driven by the MRI develops by orbit 3 ($t \approx 10$ ms), starting the radial spread of the disk due to sustained angular momentum transport. Concurrent with the onset of accretion, a relativistic outflow is launched around the rotation axis due the magnetic pressure gradient generated by field winding in the vicinity of the black hole (e.g., Hawley & Krolik 2006). In our model, this expansion occurs on a few orbital times (Figure 3). Thereafter, the polar outflow is composed of an inner, magnetically dominated jet around the rotation axis, and an outer matter-dominated outflow around it (as described in, e.g., De Villiers et al. 2005).

The entropy in the disk is such that electrons are mildly degenerate, resulting in an equilibrium electron fraction $Y_e \lesssim 0.1$ (equation 9), not very different from the initial value. Before the onset of the MRI, neutrino cooling decreases the entropy and thus the equilibrium electron fraction except at the location of the current sheet, where dissipation results in heating and an increase in Y_e (Figure 3). The onset of the vertical outflow removes low- Y_e material from the neutronized core of the disk and spreads it to large radii. Once the disk becomes turbulent, the temperature increases in the inner regions, and higher Y_e material is launched along the outer wall of the axial funnel. The spatial distribution of Y_e in this early outflow is shown in Figure 4.

3.1.1 Comparison with hydrodynamic models

In contrast to the GRMHD model, hydrodynamic models display a mostly laminar evolution throughout this time period, as shown in Figure 5 for the model with $\alpha = 0.1$ (h2d-v10). The absence of magnetic fields, the event horizon, and general relativistic frame dragging precludes the generation of a relativistic outflow in the polar direction. Angular momentum transport by the azimuthal shear stress causes the disk to begin accreting around orbit 1 while simultaneously spreading the disk outward on its rear side. The GRMHD model does not begin this outward equatorial expansion until the MRI is fully developed (Figure 3). The overall geometry of the early outflow therefore differs significantly when including magnetic fields, as illustrated in Figure 4. By 10 ms after the onset of the simulation, the hydrodynamic model remains spheroidal, while the GRMHD has already expanded into a hour-

glass shape with an approximately 3:1 ratio between vertical and horizontal dimensions.

The hydrodynamic model is subject to viscous heating from the beginning, and therefore its temperature is higher than the GRMHD model during the first few orbits, before the MRI-driven turbulence has time to develop. This results in an entropy difference between the two models, and therefore in a different level of electron degeneracy and equilibrium electron fraction (equation 9). The hydrodynamic model gradually raises its Y_e throughout the disk, particularly in regions above the equatorial plane and close to the inner edge of the disk, where the temperature is high and the density is low. If the initial magnetic field at the time of torus formation is already turbulent (as found in, e.g., Kiuchi et al. 2014), then the early thermal evolution of the disk might be closer to the hydrodynamic models due to the enhanced energy deposition from turbulent dissipation (with implications for the composition of the early outflow).

3.2 Long-term evolution, accretion history, and energy output

As the disk starts accreting onto the BH and spreading due to angular momentum transport, the average density decreases while the temperature remains nearly constant at a fixed position, thereby gradually increasing the disk entropy, decreasing the electron degeneracy, and thus increasing the equilibrium value to which weak interactions drive Y_e . This change is visible in Figure 3 through the shrinking of the 10^9 g cm^{-3} density contour and the increase in Y_e over $\sim 10 - 100$ orbits ($\sim 30 - 300$ ms). The disk therefore starts ejecting material with increasingly higher electron fraction, as visible from Figure 4. This process operates in both GRMHD and hydrodynamic models, as shown in Figure 5.

The continued decrease in the density eventually causes weak interactions to drop to dynamically unimportant levels, thus freezing out Y_e . This transformation from a neutrino-cooled disk (Popham et al. 1999; Chen & Beloborodov 2007) to an advection-dominated accretion flow (Narayan & Yi 1994) occurs on the angular momentum transport timescale (Beloborodov 2008; Metzger et al. 2009). This transition can be quantified by the evolution of the total neutrino and antineutrino luminosity

$$L_\nu = \int \rho u_r Q \sqrt{-g} dx^r dx^\theta dx^\phi, \quad (33)$$

shown in Figure 6. The GRMHD model becomes advective over ~ 300 ms, or about 100 orbits.

To further diagnose our models, we compute the rest mass

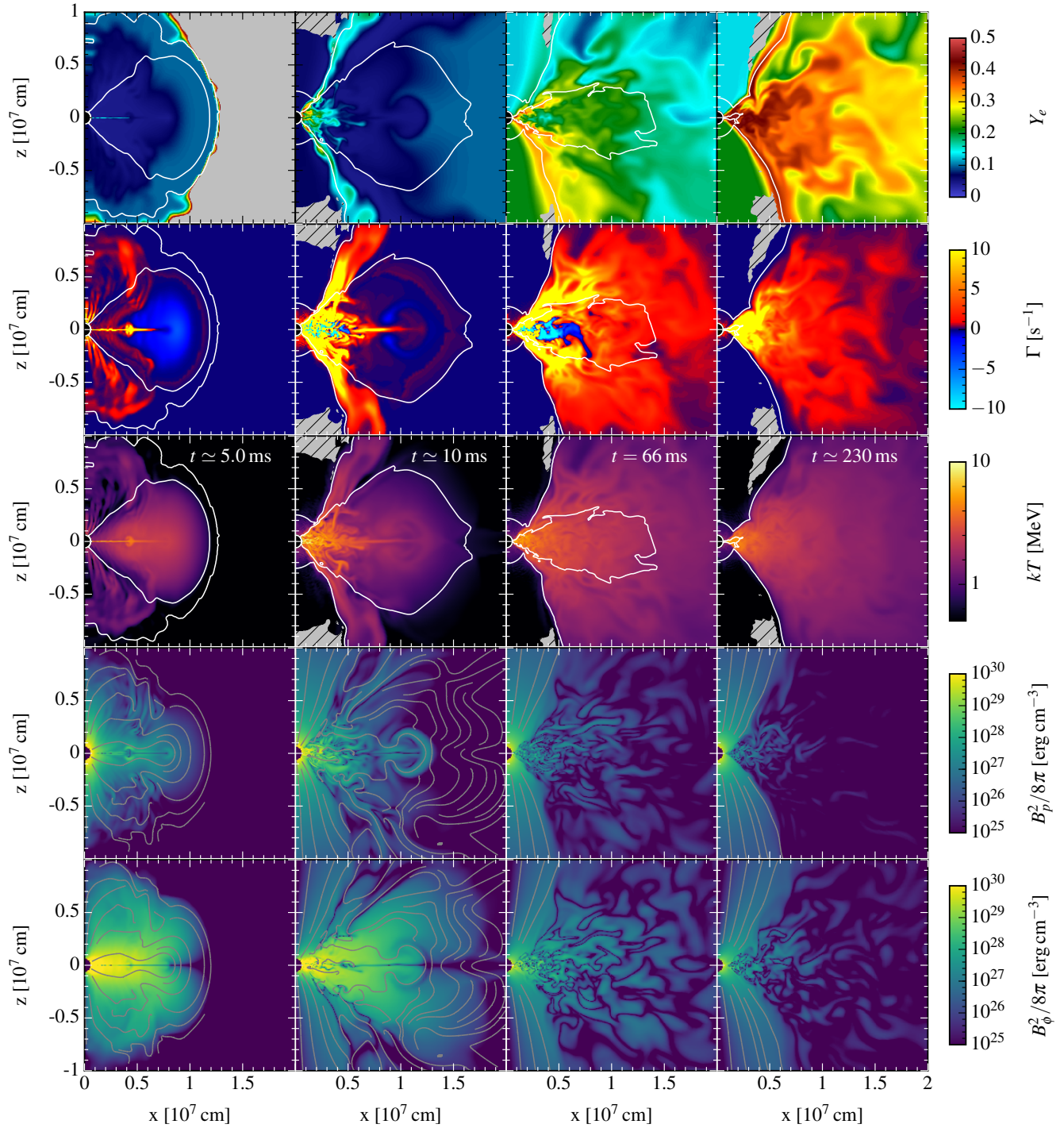


Figure 3. Snapshots of the early evolution of the GRMHD model (slice $y = 0$), with each column corresponding to the time as labeled in the middle row (the orbital time at the initial density peak is 3.3 ms, or $224r_g/c$). From top to bottom, rows correspond to electron fraction, neutrino number source term Γ (equation 3), temperature, poloidal magnetic pressure, and toroidal magnetic pressure, respectively. The white contours correspond to mass densities of 10^6 g cm^{-3} (outer) and 10^9 g cm^{-3} (inner), and some magnetic field lines are shown in gray in the lower two rows. The gray hatched area corresponds to regions excluded from our analysis for having high magnetization or a density close to the floor value (§2.4).

flow rate at a given radius in the GRMHD model using

$$\dot{M}(r) = \oint \rho u^r \sqrt{-g} dx^\theta dx^\phi. \quad (34)$$

Similarly, the surface integral of the energy flux in the GRMHD

model is obtained from the stress-energy tensor

$$\dot{E}(r) = - \oint T_r^t \sqrt{-g} dx^\theta dx^\phi. \quad (35)$$

Following McKinney et al. (2012), we compute the kinetic, en-

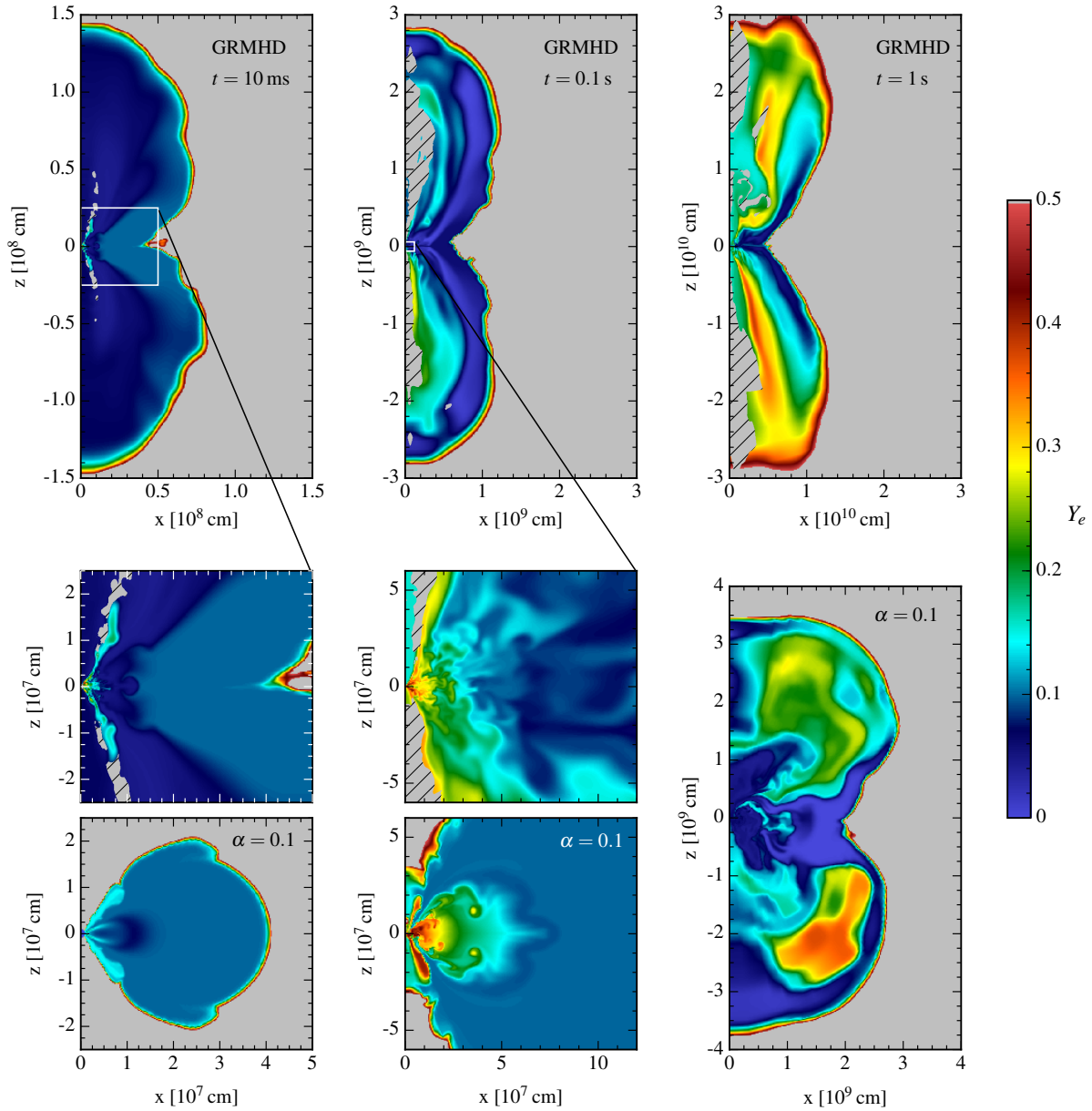


Figure 4. Snapshots of the electron fraction in the GRMHD model (slice $y = 0$, top and middle panels) and in the hydrodynamic model with $\alpha = 0.1$ (bottom panels) at times $t = 10$ ms (left), 100 ms (center), and 1 s (right). The two leftmost panels in the middle row are zoom-ins of the corresponding panels in the top row. Note the difference in scale between panels. The gray hatched region in the GRMHD model is excluded from the analysis for having high magnetization or density close to the floor value (§2.4).

thalpy, and electromagnetic components separately:

$$\dot{E}_k(r) = - \oint \rho u^r (1 + u_r) \sqrt{-g} dx^\theta dx^\phi \quad (36)$$

$$\dot{E}_{\text{th}}(r) = - \oint (\epsilon + P) u^r u_r \sqrt{-g} dx^\theta dx^\phi \quad (37)$$

$$\dot{E}_{\text{EM}}(r) = - \oint [(b^\mu b_\mu) u^r u_r - b^r b_r] \sqrt{-g} dx^\theta dx^\phi, \quad (38)$$

respectively, where the notation follows the unit system of §2.2⁵. The rest mass power output at a given radius is $\dot{M}(r) c^2$.

⁵ The integrals are carried out in code units and the result is multiplied by $M_{\text{bh}} c^3 / r_g$ to convert to physical units.

The rest mass accretion history at the ISCO radius is shown in Figure 7. The mass flow into the BH reaches a peak around the time MRI turbulence develops (c.f. Figure 3), subsequently decreasing in intensity by almost five orders of magnitude by $t \approx 10$ s. The total mass accreted in the GRMHD model is $0.02 M_\odot$, or $\approx 60\%$ of the initial torus mass.

The different components of the power at a radius $r_{\text{out}} = 10^9 \text{ cm} \approx 2,000 r_g$ are shown in Figure 8. The rest mass energy output dominates over all other components. The kinetic power dominates over the electromagnetic power throughout the disk evolution. We analyze more closely the mass ejection process and the properties of the ejecta in §§3.3-3.4. The electromagnetic power output peaks at early times, when the magnetized outflow generated dur-

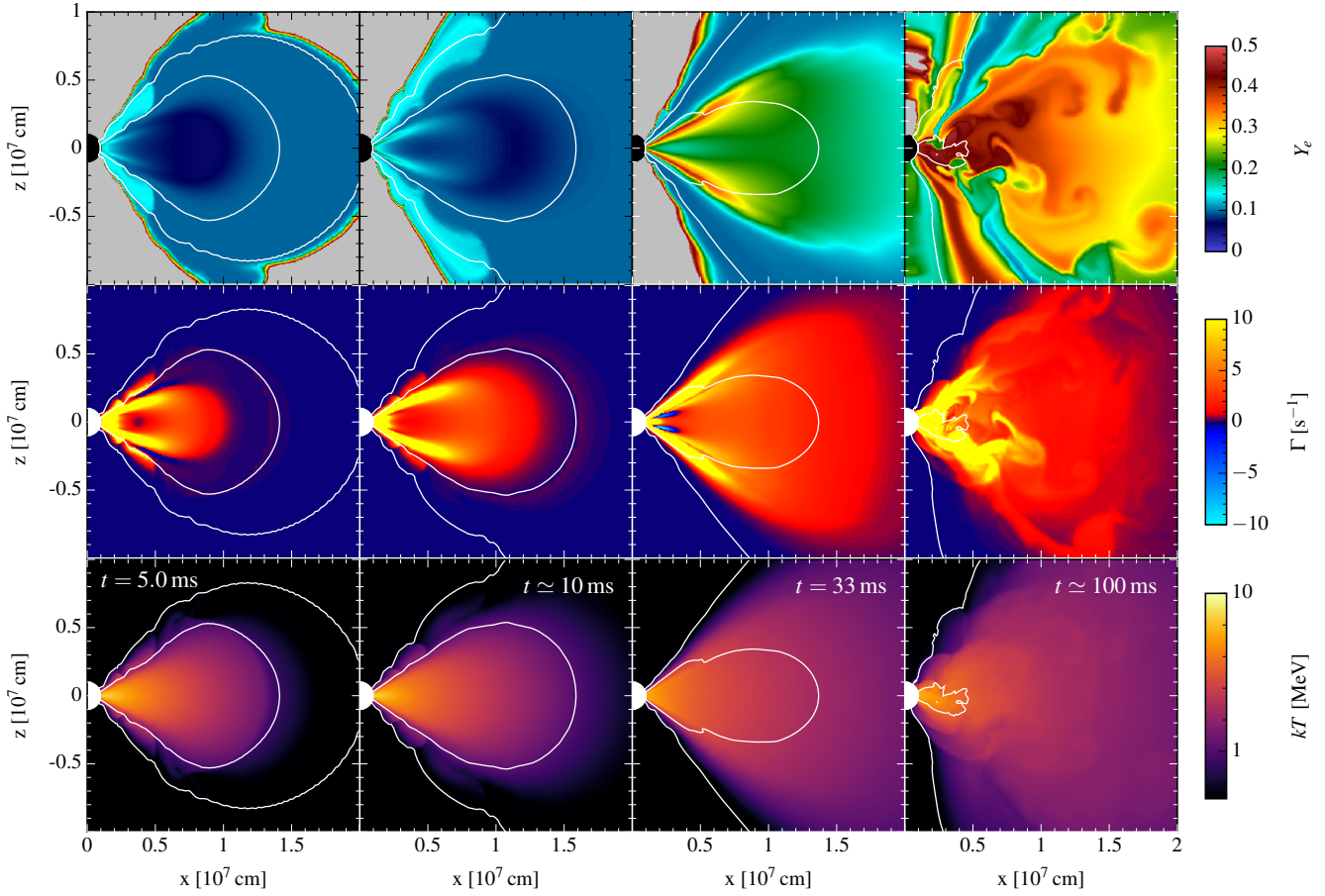


Figure 5. Same as Figure 3, but for the hydrodynamic model with $\alpha = 0.1$.

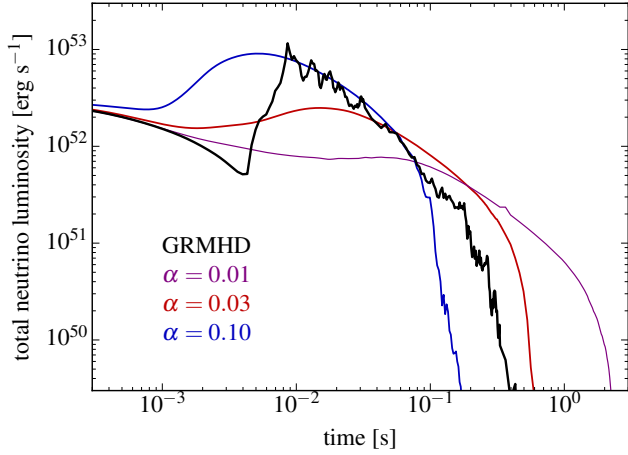


Figure 6. Total neutrino and antineutrino luminosity (equation 33) as a function of time for the GRMHD model and the three hydrodynamic models with different values of the viscosity parameter, as labeled. For reference, each second of physical time corresponds approximately to $6.7 \times 10^4 r_g/c$.

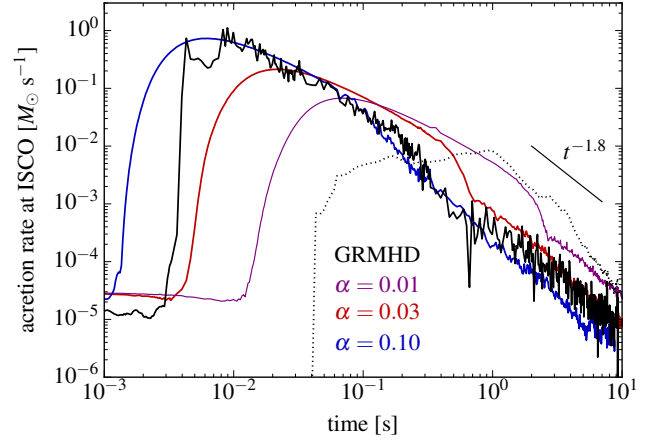


Figure 7. Rest-mass accretion rate (equation 34) at the ISCO radius as a function of time for the GRMHD model and the hydrodynamic models with varying viscosity. The dotted black line shows the mass outflow rate at 10^9 cm for the GRMHD model (c.f. Figure 9). A power-law fit to the GRMHD accretion rate gives $t^{-1.8}$ for $t > 1$ s, while the time dependence for both hydrodynamic models with $\alpha = 0.03 - 0.1$ is $t^{-1.9}$ s.

ing the early disk evolution (§3.1 and Figure 3) reaches $r = r_{\text{out}}$. The total energy carried by the Poynting jet (in all directions) is

$\sim 3 \times 10^{50}$ erg over the duration of our simulation⁶. A power-law

⁶ The total energy generated by the jet depends on our choice of high-

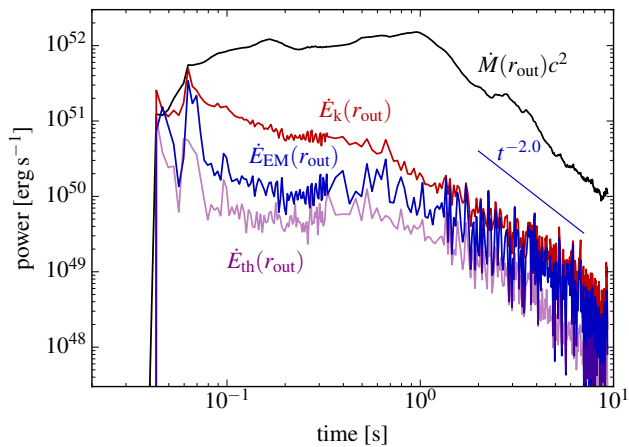


Figure 8. Power generated by the GRMHD model at a radius $r_{\text{out}} = 10^9$ cm $\approx 2,000r_g$, separated into components (rest mass, kinetic, electromagnetic, and thermal) according to equations (34) and (36)-(38). The blue line shows a power-law fit to the electromagnetic power for $t > 1$ s.

fit to $\dot{E}_{\text{EM}}(r_{\text{out}})$ yields t^{-2} for $t > 1$ s, roughly following the time-dependence of the mass accretion rate.

3.2.1 Comparison with hydrodynamic models

The luminosity and mass flow rate for the hydrodynamic models is computed using equations (33) and (34) with $u_t = -1$, $\sqrt{-g} = r^2 \sin \theta$, and $(x^r, x^\theta, x^\phi) = (r, \theta, \phi)$. Figure 6 shows that the early evolution of L_ν in the GRMHD model deviates somewhat from that of all the hydrodynamic models due to the delayed onset of angular momentum transport by the MRI relative to the viscous stress (§3.1). At late-times, the neutrino emission from the GRMHD model is bracketed by that of the hydrodynamic models with $\alpha = 0.03 - 0.1$.

As with the neutrino luminosity, the late-time accretion history of the GRMHD model is bracketed by the hydrodynamic models with $\alpha = 0.03 - 0.1$. A power-law fit to the accretion rate in the GRMHD model for $t > 1$ s yields $t^{-1.8}$, while in the hydrodynamic models with $\alpha = 0.03 - 0.1$ the dependence is $t^{-1.9}$. Despite the different treatment of gravity and processes driving angular momentum transport, the temporal slope of the mass accretion rate at late times is essentially the same in all models.

The main difference between the accretion histories of GRMHD and hydrodynamic models has to do with the level of stochasticity of the fluid reaching the BH. Given that MRI-driven turbulence transports angular momentum, mass flow onto the BH in the GRMHD model shows fluctuations throughout its evolution. In contrast, accretion is smooth for the hydrodynamic models for as long as neutrino cooling is important. Around the time when weak interactions freeze out, the magnitude of the accretion rate drops from its initial power-law evolution and becomes stochastic, latching onto a different power-law trajectory. While the GRMHD models does not display such a marked transition in its accretion history, fluctuations in the accretion rate show a visible modification around $t \sim 300$ ms, when neutrino cooling becomes unimportant.

magnetization and low-density cut (§2.4). Removing our cut increases the electromagnetic energy output to 1.3×10^{51} erg.

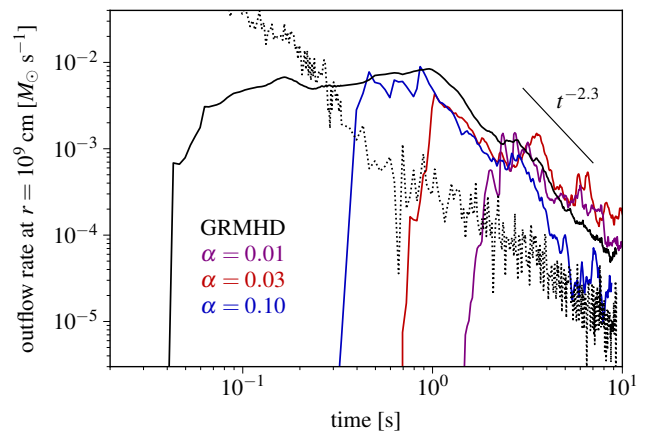


Figure 9. Rest-mass unbound outflow rate (equation 34 restricted to $-hu_t > 1$) at $r_{\text{out}} = 10^9$ cm as a function of time for the GRMHD model (solid black line). A power-law fit to this mass-loss rate yields $t^{-2.3}$ for $t > 1$ s. For comparison, we also show the outflow rates for the three hydrodynamic models with varying α , as labeled. The dotted line shows the mass accretion rate at the ISCO for the GRMHD model (c.f. Figure 7), and the gray shaded area shows the fraction of the outflow in the GRMHD model that satisfies the condition $-u_t > 1$.

3.3 Mass ejection

The total amount of unbound mass ejected at a radius of 10^9 cm is shown in Table 1. In the GRMHD model, matter is considered to be unbound when it satisfies the condition $-(1 + \gamma_{\text{ad}}\epsilon/\rho)u_t = -hu_t > 1$. This condition corresponds to a positive Bernoulli parameter in Newtonian gravity, accounting for the internal energy available for conversion to kinetic energy via adiabatic expansion upon subsequent evolution. For comparison, we also use the more restrictive ‘geodesic’ condition $-u_t > 1$, which corresponds to demanding that the escape speed be locally exceeded in Newtonian gravity, thus providing a lower limit on mass ejection (e.g., Kas-taun & Galeazzi 2015; Bovard et al. 2017). The radius of 10^9 km ($\approx 2,000r_g$) is chosen such that most of the outflow can be measured before the outer edge of the disk spreads to that point.

The GRMHD model ejects about $1.3 \times 10^{-2} M_\odot$, or 39% of the initial torus mass. The mass ejection history at $r = 10^9$ cm is shown in Figure 9. The initial outflow reaches this radius by a time of ~ 40 ms, as can be seen from Figure 4. This early outflow plateaus at a time of ~ 0.1 s, then slowly increases to a peak at $t \sim 1$ s. Thereafter, mass ejection decreases sharply with time, following a $t^{-2.3}$ dependence. By $t = 9.3$ s the mass outflow rate is a factor 300 lower than at its peak. At the end of the simulation, the rate of change of the cumulative ejected mass satisfies $d \ln M_{\text{ej}}/d \ln t \approx 0.03$, thus **mass ejection is complete to within other uncertainties**.

Using the more restrictive ‘geodesic’ criterion to determine the gravitational binding of the outflow results in only 30% of the disk mass being ejected. Figure 9 shows that nearly all the decrease (compared to the Bernoulli criterion) arises in the late-time phase of the outflow, after $t = 1$ s. At this time most of the material is ejected thermally by nuclear recombination and dissipation of MHD turbulence given the absence of neutrino cooling (§3.4.3). Since material is ejected from larger radii in this phase, the outflow has not yet undergone full adiabatic expansion and retains significant thermal energy at a radius 10^9 cm. The gravitational binding criterion does not affect the total kinetic or electromagnetic energy of the outflow.

Instead, these quantities are dependent on the magnetization and low-density cut (§2.4).

The physics of the polar unbound outflows in three-dimensional GRMHD simulations of accretion disks around spinning black holes has been studied by De Villiers et al. (2005) and Hawley & Krolik (2006). They found that the jet core is magnetically-dominated, with a very low matter density, and contains field lines that are primarily radial, with a degree of coiling that depends on the spin of the black hole. Matter outflow was found to reside outside the jet ‘wall’, being confined from the jet side by centrifugal forces and on the outside by gas pressure from the disk corona. When inspecting the effective gravitational potential, Hawley & Krolik (2006) found that while centrifugal forces help direct the matter outflow, they do not accelerate it. Instead, they argued that the combination of gas and magnetic pressure gradients in the corona provide a suitable acceleration mechanism. Besides the narrow region around the jet wall, no unbound matter outflows were found, with bound coronal ‘backflows’ closer to the equatorial plane.

While our GRMHD model displays many of the features described in Hawley & Krolik (2006), important differences arise. The accretion disk transitions from being neutrino cooled at times $t \lesssim 100$ ms ($\sim 10^4 r_g/c$) to being advective, and recombination of nucleons into alpha particles (equation 10) provides an additional source of energy for unbinding material at all angles. Siegel & Metzger (2018) have in fact argued that nuclear recombination is the key process behind unbound mass ejection when including MHD.

Early mass ejection is confined to latitudes close to the rotation axis, and a configuration of an empty jet funnel plus matter wall is indeed present. However, the matter outflow expands sideways significantly, wrapping around behind the back of the disk (c.f. Figure 4). The disk itself spreads outward along the equatorial plane due to angular momentum transport, and eventually also ejects mass from its side opposite to the black hole. Most of the disk nevertheless remains gravitationally bound, and at late times ($\gtrsim 1$ s) some of this bound material makes its way outwards through latitudes close to the equatorial plane. At the end of the simulation, only $\lesssim 1\%$ of all the matter reaching a radius of 10^9 cm is gravitationally bound.

3.3.1 Comparison with hydrodynamic models

For hydrodynamic models, we consider fluid with positive specific energy to be unbound. These models eject 16 – 22% of the initial disk mass in unbound material, with larger ejecta for increasing viscosity parameter. The magnitude of this mass ejection and its dependence on the viscosity parameter is consistent with previous hydrodynamic simulations of disks around spinning black holes (e.g., Just et al. 2015; F15). Figure 9 shows that the outflow starts much later than in the GRMHD model, but exhibits a very similar temporal dependence once peak mass ejection has been reached around a time of 1 s. As is the case with the neutrino luminosity and accretion rate at the ISCO, the hydrodynamic models with $\alpha = 0.03$ and $\alpha = 0.1$ bracket the mass ejection history of the GRMHD model.

The difference in mass ejected and early temporal dependence between GRMHD and hydrodynamic models arises from the absence of magnetically-driven outflows at early times in the hydrodynamic models. In fact, the amount of mass ejected before 1 s in the GRMHD model is about one half of the total: 19% of the initial torus mass before 1 s, and 20% thereafter. The latter is comparable to the mass ejected by the hydrodynamic models.

The primary mass ejection mechanism in the hydrodynamic models operates during the advective stage, when viscous heating exceeds neutrino cooling (e.g., Metzger et al. 2009; Lee et al. 2009; Fernández & Metzger 2013a). Angular momentum transport moves material to shallower regions of the gravitational potential, from where energy injection by viscous heating and alpha particle recombination can unbind it. This accounts for the late-time onset of mass ejection relative to the GRMHD model. Mass ejection due to neutrino absorption (not included in our simulations) is subdominant when a black hole is the central object (c.f. Just et al. 2015).

3.4 Outflow properties

The distribution of electron fraction, entropy, and radial velocity in the outflow at $r = 10^9$ is shown in Figure 10 for the GRMHD model. Histograms are constructed by considering only unbound matter and excluding regions with high magnetization and density close to the floor value (§2.4).

The early phase of mass ejection in the GRMHD model is mostly neutron-rich ($Y_e \lesssim 0.2$) and fast ($v^r/c > 0.1$). As time elapses, material with increasing electron fraction and lower velocities enters the outflow up to about 1 s of evolution. At later times, the trend toward lower velocities continues but the mean Y_e decreases back to 0.1 – 0.2. The final electron fraction distribution spans the range 0.03 – 0.4, and the outflow velocity extends from $10^{-3}c$ up to relativistic motion. The average values are $\langle Y_e \rangle = 0.16$ and $\langle v^r/c \rangle = 0.11$ (Table 1).

The entropy of the outflow⁷ is quantified by assuming that all matter species follow an ideal gas distribution, consistent with our calculation of the temperature via equation (2):

$$s = \left[\frac{5}{2} - \ln \left(\frac{n}{n_Q} \right) \right] \left[1 + Y_e - \frac{3}{4} X_\alpha \right] + \frac{4}{3} \frac{aT^3}{nk_B} - \left[Y_e \ln \left(Y_e \left[\frac{m_n}{m_e} \right]^{3/2} \right) + X_n \ln X_n + X_p \ln X_p + \frac{1}{4} X_\alpha \ln \left(\frac{X_\alpha}{32} \right) \right], \quad (39)$$

where $n = \rho/m_n$ is the baryon number density. Figure 10 shows that the entropy distribution of the GRMHD simulation peaks in the range 20 – 30 k_B per baryon, and has an extended tail to high values. This general shape is maintained throughout the evolution.

The origin of the high-entropy tail becomes clear when inspecting Figure 11. The bulk of the ejecta at mid-latitudes and on the equatorial plane has entropies below 100 k_B per baryon. Much larger values are obtained around the jet head and funnel, and at the interface between the outflow and the ambient medium. The low densities involved result in large entropies due to the radiation term $\propto T^3/\rho$ in equation (39), which dominates in this regime. Given that our numerical method has limited validity in highly magnetized regions close to the density floor, the results need to be interpreted with caution. For instance, the detailed form of the high-entropy tail of the distribution is sensitive to our cut in magnetization and density (§2.4).

⁷ The entropy is commonly used as one of the parameters that describes the r -process. Since the conditions during nucleosynthesis are usually radiation-dominated, the entropy directly quantifies the number density of photons and thus the strength of photodissociation, which is expected to balance neutron capture along the r -process path (Meng-Ru Wu & Stéphane Goriely, private communication).

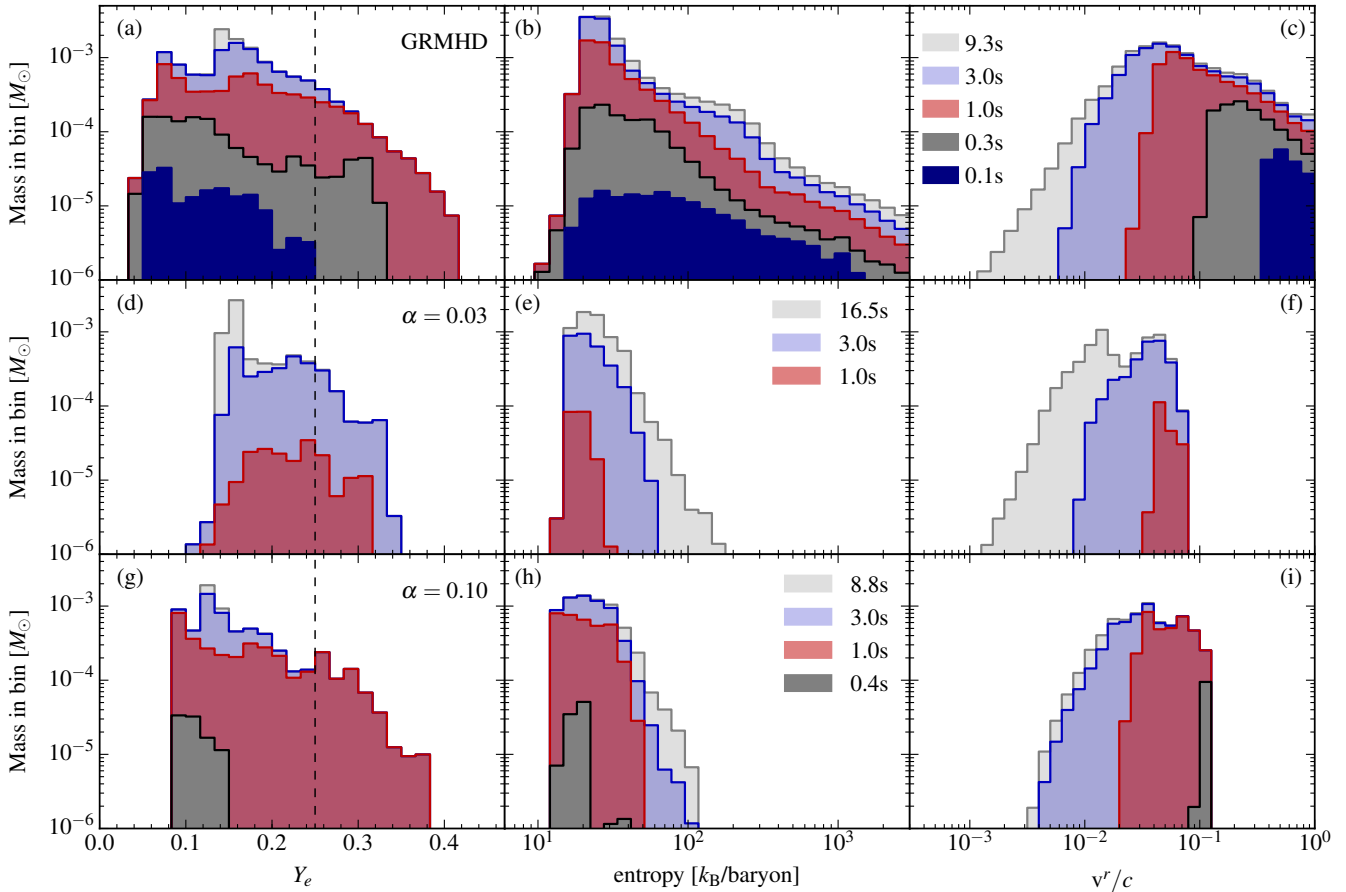


Figure 10. Histograms of unbound ejected mass as a function of electron fraction (left column), entropy (middle column; equation 39), and radial velocity v^r (right column), measured at $r = 10^9$ cm, for the GRMHD model (top row), and the hydrodynamic models with $\alpha = 0.03$ (middle row), and $\alpha = 0.1$ (bottom row). Colors denote cumulative values at selected times, as labeled. The vertical dashed line marks the approximate boundary between lanthanide-rich ($Y_e < 0.25$) and lanthanide-poor material (e.g., Kasen et al. 2015). The bin sizes are $\Delta Y_e = 0.017$, $\Delta \ln s = 1.26$, and $\Delta \ln(v^r/c) = 1.31$.

3.4.1 Comparison with hydrodynamic models

Figure 10 also shows histograms for the hydrodynamic models that show the closest similarity to the GRMHD model at late times. These models display a somewhat narrower distribution of electron fraction relative to the GRMHD model, with a lower limit close to the initial value of $Y_e = 0.1$. At the high- Y_e end, increasing viscosity results in a tail extending to increasingly higher Y_e , even though the average of the distribution is lower (Table 1).

The velocity distribution of the hydrodynamic models cuts off sharply around $v_r/c \sim 0.1$, with a lower velocity tail that follows a power-law similar to the GRMHD model. The cutoff value at high speed corresponds to the (Newtonian) escape speed at ~ 500 km, which is larger than the radius of the initial density peak by a factor ~ 10 . A larger radius of ejection is expected from the spreading of the disk in hydrodynamics prior to the freezeout of weak interactions. Also, the cutoff is consistent with the maximum velocity that can be obtained from the recombination of alpha particles, $\sqrt{2B_\alpha/m_\alpha} \approx 0.12c$.

The low-entropy peak in the GRMHD model is similar to the entropy distribution of the hydrodynamic models, and is thus expected if the ejection timescales and thermodynamic properties of the outflow are similar (§3.4.3).

3.4.2 Relativistic Ejecta and Angular Distribution

A small fraction of the ejecta from the GRMHD model achieves Lorentz factors $\sim 1 - 10$. Figure 12 shows the final kinetic energy and mass histograms as a function of normalized relativistic momentum⁸ $\gamma\beta$. While most of the mass has sub-relativistic velocity ($\langle\gamma\beta\rangle \approx 0.14$ weighted by mass), most of the kinetic energy of the outflow is carried by mildly relativistic material ($\langle\gamma\beta\rangle \approx 1.8$ weighted by kinetic energy). As shown by Figure 8, the kinetic power exceeds the electromagnetic power of the jet during most of the disk evolution. Note that the detailed shape of the kinetic energy distribution for $\gamma\beta \gtrsim 3$ is set by our choice of high magnetization and low density cut (§2.4) when constructing it, as shown in Figure 12. The mass distribution, on the other hand, is rather insensitive to our choice of cut.

Figure 12 also shows the reverse-cumulative distribution of kinetic energy $E_k(> \gamma\beta)$ and of mass $M_{\text{ej}}(> \gamma\beta)$. The former has been used as an input to models that fit the non-thermal emission from GW170817 (e.g., Hotokezaka et al. 2018). Comparing with the fit of Mooley et al. (2018), our GRMHD model contains too much kinetic energy to account for the non-thermal emission when

⁸ Not to be confused with the adiabatic index γ_{ad} or the ratio of gas pressure to magnetic pressure β_{pl} .

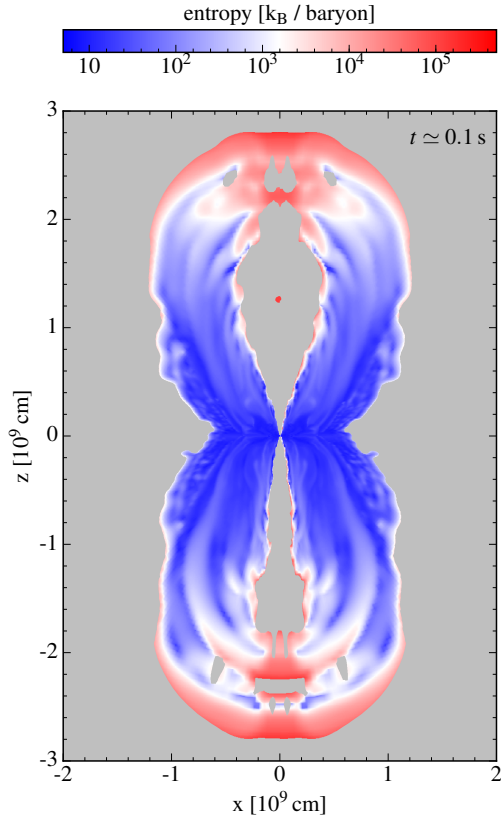


Figure 11. Snapshot of the entropy (equation 39) in the GRMHD model at time $t \approx 0.1$ s. The slice is perpendicular to the y -axis. The gray-shaded region corresponds to regions excluded from our analysis for having high magnetization or a density close to the floor value (§2.4).

considered as a spherical blast wave. Note however that the kinetic energy distribution is expected to change, as the fastest component of the disk outflow will catch up with the dynamical ejecta and interact with it.

The non-thermal emission from GW170817 can also be produced by a jet viewed off-axis, which has an angle-dependent Lorentz factor (a ‘structured jet’, e.g. Haggard et al. 2017; Lazati et al. 2018; Margutti et al. 2018). Figure 13 shows histograms of mass, kinetic energy, and average relativistic momentum as a function of polar angle relative to the rotation axis. The average is computed using both the mass and kinetic energy distributions as weights. The former yields a lower value than the latter, as expected from the momentum distributions shown in Figure 12.

Most of the kinetic energy of the outflow is concentrated in directions close to the polar axis. The angular bins closest to the north and south directions ($\sim 21^\circ$ in size) contain nearly all of the kinetic energy of the outflow, approximately⁹ 8×10^{50} erg. Moving away from the axis results in a very steep decrease in the kinetic energy, with the equatorial direction being lower than the poles by a factor of ~ 1000 . This focusing of fast material along the polar direction is also reflected in the angular distribution of relativistic momentum, both mass- and kinetic-energy-weighted.

In contrast, mass ejection shows a significant pole-equator anisotropy only at early times $t \lesssim 0.3$ s, with subsequent mass ejection

⁹ Removing the high-magnetization and low-density cut increases the total kinetic energy of the jet to 1.1×10^{51} erg.

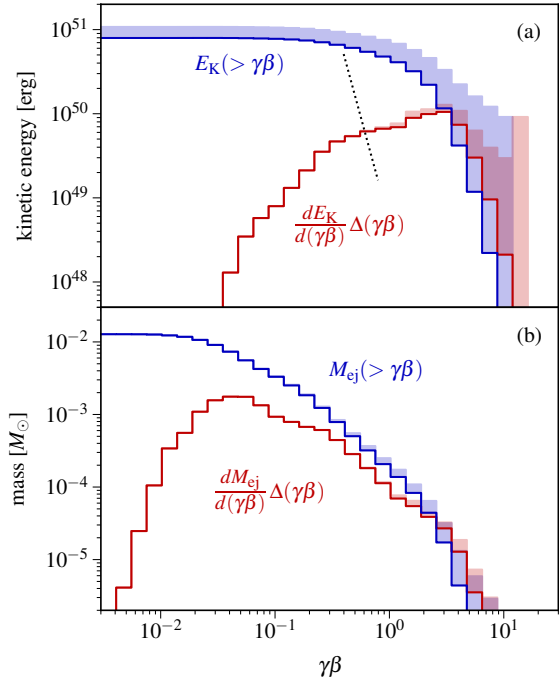


Figure 12. Final histograms of kinetic energy (top) and unbound mass ejected (bottom) as a function of relativistic momentum for the GRMHD model, as measured at $r = 10^9$ cm. In both cases, a quantity per bin and a reverse-cumulative version is shown (the bin size is $\Delta \ln \gamma\beta = 1.36$). The dotted line is the spherical blast wave fit to the non-thermal emission from GW170817 by Mooley et al. (2018), $E(> \gamma\beta) = 5 \times 10^{50} (\gamma\beta/0.4)^{-5}$ erg. The shaded areas indicate the results obtained when removing our low-density and high-magnetization cut (§2.4).

turning the distribution quasi-spherical, with a pole-to-equator anisotropy of approximately 2 : 1 by the end of the simulation.

For comparison, Figure 13 also shows the structured jet fit of D’Avanzo et al. (2018) for the isotropic equivalent energy of GW1710817, $E(\theta) = (\Delta \cos \theta/2) 10^{52} / (1 + [\max(\theta, 2^\circ)/2^\circ]^{3.5})$ erg, where the prefactor normalizes the isotropic equivalent energy to the angular bin size $\Delta \cos \theta$. When considered over the entire range of polar angles, the functional form of the fit has a much steeper decay with polar angle than implied by our angular histogram. The inset of Figure 13 shows a zoom-in on the angular distribution of all emitted forms of energy close to the axis. While the outflow generated in our GRMHD model produces too much kinetic energy relative to the non-thermal emission of GW170817, the angular dependence of the kinetic, electromagnetic, and thermal components is compatible with the fit of D’Avanzo et al. (2018). Again, we caution that the fastest component of the disk outflow will almost certainly interact with the dynamical ejecta and therefore the kinetic energy distribution will change relative to that shown in Figure 13 (§3.6)

3.4.3 Mass Ejection in the Advective Stage

Given that about half of all mass ejection by the GRMHD model reaches our fiducial radius r_{out} after 1 s, and that the subsequent evolution of the mass ejection history (Figure 9) is similar to that of the hydrodynamic models, it is worth exploring whether the properties of mass ejection are similar in the GRMHD and hydrodynamic models once neutrino cooling has subsided.

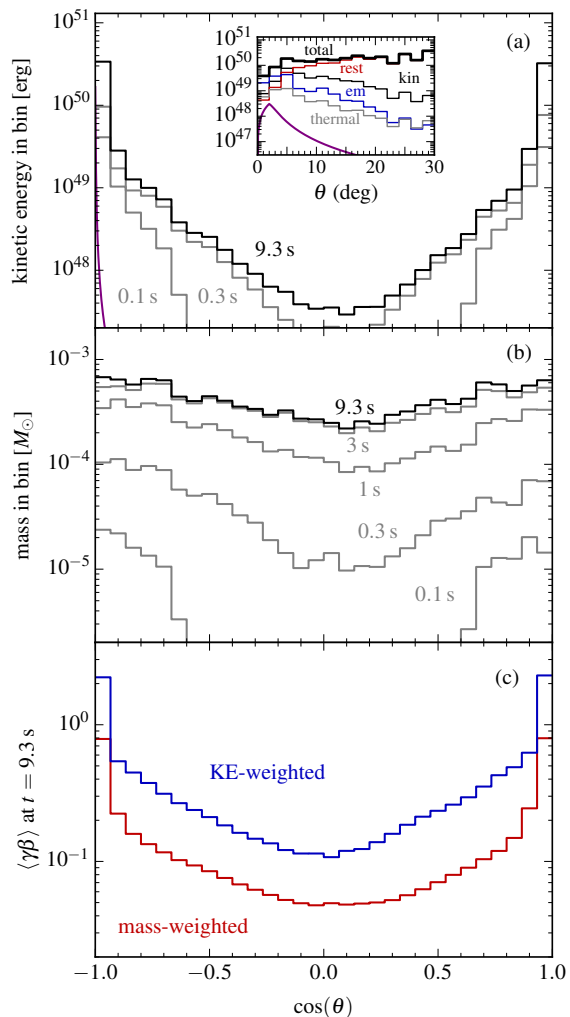


Figure 13. Histograms of kinetic energy (top), unbound mass ejected (middle), and average relativistic momentum (bottom) as a function of $\cos\theta$ for the GRMHD model, as measured at $r = 10^9$ cm (the bin size is $\Delta\cos\theta = 0.067$; 21° at the polar axis). Black and gray solid curves in the top two panels show cumulative values at different times, as labeled. The weights for the average momentum are the mass- and kinetic energy histograms from panels (a) and (b). The purple line in the top panel shows the structured jet fit of D’Avanzo et al. (2018) to the non-thermal emission from GW170817, normalized to show energy per bin. The inset in the top panel shows energies per bin (rest mass: red, kinetic: thin black, electromagnetic: blue, thermal: grey, and total sum: thick black) as a function of polar angle close to the axis. Note that the detailed angular distribution of the relativistic ejecta will be sensitive to our choice of high-magnetization and low-density cut (§2.4).

Figure 14 shows histograms of mass ejection after 1 s in the GRMHD model (obtained by subtracting any prior contributions from the final histogram), together with the total mass histograms for the hydrodynamic model. Given that the amount of mass ejected after 1 s is comparable to that in the hydrodynamic models, we expect the amplitudes of the histograms to be similar. The late-time electron fraction distribution has the same general shape in all models, with the GRMHD model showing an overall shift to low Y_e (note that none of the models include neutrino absorption).

The late-time velocity and entropy distributions in the GRMHD model are bimodal, with the low-end distribution showing great similarity with the hydrodynamic models. Guided by the

sharp cutoff in the velocity distribution of the hydrodynamic models, we also split the late GRMHD histograms into components with velocities lower and higher than $v^r/c = 0.1$.

Figure 14 shows that the low-velocity component of the GRMHD model shows excellent agreement with the hydrodynamic models, pointing to an underlying similarity in the mass ejection mechanism. The high-velocity component is also responsible for the high-entropy tail of the GRMHD histogram at late times. Given its absence in the hydrodynamic models, we surmise that it is associated with magnetic driving close to the polar axis. This association is reinforced by the Y_e distribution of this fast component, which indicates less reprocessing by neutrinos.

3.5 Comparison with previous work

The work of Shibata et al. (2007) bears the most similarity to our implementation of neutrino cooling and nuclear recombination (§2.1). Since their 2D simulations were evolved for a relatively short amount of time (60 ms) given the decay of the MRI, we can only compare their results with the earliest period in the evolution of our models. Overall qualitative agreement is found in the growth time of the MRI and the onset of accretion. Since their initial field strength is such that $\beta_{\text{pl}} = 200$ and their initial tori are more massive ($0.1 - 0.2M_\odot$) than ours, quantitative agreement in accretion rates and neutrino luminosities is not expected. Similar qualitative agreement in the early phase of MRI evolution is found with the work of Janiuk et al. (2013) and Nouri et al. (2017)

While the 2D neutrino radiation-MHD models of Shibata & Sekiguchi (2012) cannot be directly compared with our coarser implementation of neutrino physics, we can speculate about how inclusion of neutrino absorption would affect our models. Their main result is that neutrinos are emitted primarily along the polar funnel. Given that material in this region moves the fastest and therefore has a short expansion time, the effect of neutrino absorption on the overall electron fraction of the outflow might be further suppressed relative to that in hydrodynamic models when a promptly-formed BH sits at the center and the magnetic field is strong. If, on the other hand, the magnetic field is initially weak, then the additional energy deposition in the polar region can help energize a polar outflow (e.g. Just et al. 2016; Perego et al. 2017) and result in material with higher Y_e .

The work of Siegel & Metzger (2018) shows similarities and differences with ours. While their equation of state, neutrino emission, and nuclear recombination implementations are different, they find the same fraction of accreted material as we do (60% of the initial disk mass). From this number, they extrapolate their 20% of mass ejected within 400 ms into an asymptotic fraction of 40%, which is consistent with our converged results. Their disk also shows very similar accretion rates and neutrino luminosity history as ours for the first 400 ms, which is expected given the choice of disk mass and initial field strength, which is very similar as well. While their final electron fraction distribution is somewhat narrower than ours at comparable evolutionary times, most of the outflow in their model also leads to lanthanide-rich nucleosynthesis ($Y_e < 0.25$).

The main difference between our results and those of Siegel & Metzger (2018) is the significantly lower amount of ejected mass with $v^r/c > 0.25$ in their simulations (Daniel Siegel, private communication). This can be attributed in part to our choice of initial field topology (§2.4), which is optimal for the generation of magnetically-dominated outflows (Tchekhovskoy et al. 2011). Also, while their spatial resolution is comparable to ours at the ini-

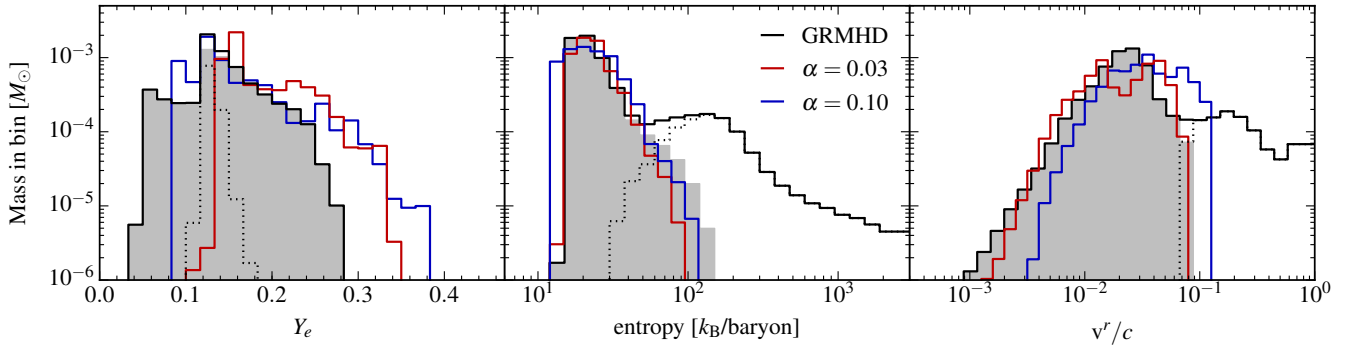


Figure 14. Mass histograms of unbound matter ejected at $r = 10^9$ cm for $t > 1$ s by the GRMHD model B3d, as a function of electron fraction, entropy, and radial velocity. The restriction to $t > 1$ s isolates outflows produced in the late-time advective phase. For comparison, the total unbound matter ejected by hydrodynamic models with $\alpha = 0.03$ and 0.1 is also shown. The gray shaded area and dashed lines denote matter with $v'/c < 0.1$ and $v'/c \geq 0.1$ in the GRMHD model, respectively. The bin sizes are the same as in Figure 10

tial torus location, our grid configuration has a factor of at least ~ 10 higher resolution at the BH horizon and can thus better capture the launching of relativistic material by magnetic fields. Other factors such as the equation of state or neutrino treatment are less likely to be important in accounting for this difference.

A larger body of literature exists on magnetized merger simulations (e.g., Rezzolla et al. 2011; Kiuchi et al. 2014; Paschalidis et al. 2015; Kiuchi et al. 2015; Ruiz et al. 2016). Given the challenging nature of these calculations, important sacrifices are normally made on the microphysics side, with implications for the thermodynamics (i.e. non-inclusion of neutrino cooling). We therefore refrain from comparing these results to ours.

3.6 Uncertainties due to initial conditions

Here we summarize the uncertainties associated with our specific choice of initial condition. Our aim in this paper is to investigate the intrinsic properties of merger remnant accretion disks when evolved in GRMHD over long timescales in a controlled setting. We have therefore employed as initial condition an equilibrium torus surrounded by a low-density ambient medium (a ‘vacuum’) and an idealized magnetic field geometry.

The most important choice we make is the initial field geometry. We have used a strong poloidal field that generates an MRI that is easiest to resolve numerically, and which yields a robust jet. A more realistic field is likely to be not only dominantly toroidal due to the merger dynamics, but also have a significant stochastic component that might enhance turbulent dissipation from the beginning (e.g., Kiuchi et al. 2014). This enhanced dissipation can modify the thermal balance and result in different initial tori entropies and composition relative to an unmagnetized merger. Purely toroidal magnetic fields have previously been found problematic to generate jets (e.g., De Villiers et al. 2005), although it might just be a matter of insufficient resolution (Liska et al. 2018). Jet-like structures have nevertheless been observed to arise from mergers of neutron stars with interior poloidal fields (Rezzolla et al. 2011; Ruiz et al. 2016).

Using a more realistic distribution of dynamical ejecta, within which the torus is immersed, is also expected to change the behavior of the outflow. The properties of the disk wind can be modified due to mixing of fallback into the disk. The results of Fernández et al. (2017) show that this admixture of neutron-rich fallback matter will result in a broader distribution of electron fraction com-

pared to evolving the disk alone. Because most of the dynamical ejecta expands faster than the late-time thermal outflow, this interplay is not expected to affect the dynamics of this component of the wind.

However, both the jet and fast component of the outflow, which can only be obtained in GRMHD, have velocities similar or exceeding that of the dynamical ejecta, and will definitely interact with it. The formation of a cocoon or even internal shocks are possible, with consequences for the electromagnetic emission (§4). Such implications must be addressed by further studies, in which the interaction between ejecta components is the main focus.

4 OBSERVATIONAL IMPLICATIONS

4.1 Kilonova

While the total ejecta mass in our GRMHD model ($0.013M_{\odot}$) is lower than that inferred from the kilonova associated with GW170817 (e.g., Kasen et al. 2017), our initial disk mass is also lower than the value expected for GW170817. Depending on the equation of state and mass ratio, numerical relativity simulations predict a disk mass in the range $0.05 - 0.2M_{\odot}$ given the total inferred mass for GW170817 (Shibata et al. 2017).

If we simply scale our ejecta to an initial disk mass of $0.1M_{\odot}$, we obtain a total ejecta mass of $0.04M_{\odot}$. Since most of the ejecta has $Y_e < 0.25$ with a mass-weighted velocity $v' = 0.11c$ (Table 1), the disk outflow can easily generate a red kilonova component similar to that from GW170817. On the other hand, the fraction of the total ejecta with $Y_e > 0.25$ is too small to account for the blue kilonova component. Performing the same scaling to a disk of mass $0.1M_{\odot}$ would yield $3.6 \times 10^{-3}M_{\odot}$ of lanthanide-poor ejecta, which is lower by almost an order of magnitude relative to the required value.

We caution, however, that these higher disk masses would be more opaque to neutrinos, so it is probably not quantitatively accurate to simply scale the results of our simulations to higher disk masses. Also, the mass estimates from kilonova fits assume that the blue and red components evolve independently of each other; proper radiation transport of the entire ejecta can yield different inferred ejecta masses (Kawaguchi et al. 2018). Figure 4 shows that there is some degree of spatial stratification in the electron fraction in addition to the non-spherical distribution of ejecta, both of which can generate a viewing angle dependency for the kilonova.

On the positive side, the average radial velocity of the lanthanide-poor material ($v^r = 0.22c$) is consistent with that from the blue kilonova from GW1710817.

A small amount of lanthanide-poor mass ejected by a disk around a promptly-formed BH is consistent with previous hydrodynamic disk models (Fernández & Metzger 2013a; Just et al. 2015; F15). This has been used as an argument for a non-zero lifetime of the HMNS in GW170817, which would irradiate the ejecta with neutrinos and increase the electron fraction (Metzger & Fernández 2014; Perego et al. 2014; Fujibayashi et al. 2018), resulting in a larger ejecta mass with $Y_e > 0.25$. Previous simulations of disks around HMNSs find average outflow velocities that do not significantly exceed $0.1c$, however, in conflict with the high velocity of the blue kilonova from GW170817. A strongly-magnetized HMNS can produce faster outflows (e.g., Kiuchi et al. 2012; Siegel et al. 2014), resolving this tension (Metzger et al. 2018). Our results show that this increase in outflow velocity is also realized in GRMHD models of BH accretion disks, as the effects of magnetic stresses, turbulent energy dissipation, nuclear recombination (and significant neutrino heating in the case of a HMNS) can all act in concert to accelerate matter.

4.2 Neutron Precursor

Mass with $v^r \sim c$ can generate strong early (\sim hr timescales) thermal emission powered by the radioactive decay of free neutrons left over after the r -process completes (Metzger et al. 2015). To avoid capturing neutrons, the ejecta must have an expansion time shorter than about 5 ms (Goriely et al. 2014; Just et al. 2015).

Given that our disk models achieve temperatures of 5×10^9 K (onset of nucleosynthesis) at radii $\sim 5 \times 10^7$ cm (e.g., Wu et al. 2016), the required expansion times are achieved for velocities $v^r \gtrsim 0.3c$. Using a conservative lower limit of $0.4c$, we find that about $7.4 \times 10^{-4} M_\odot$ of the GRMHD disk outflow (about 2% of the initial disk mass) achieves the required velocities. Figures 10 and 14 also show that the fastest ejecta has a significant neutron fraction at both early and late times. This amount of mass is comparable to or larger than the fraction of the dynamical ejecta found by Bauswein et al. (2013) to meet the conditions for a free neutron outflow. It is thus possible that the disk outflow is critical for understanding the thermal emission from NS mergers on hour timescales. Note however that a neutron-powered precursor from the disk outflow would require that the material is not obscured by opaque dynamical ejecta in front of it, thus realistic initial conditions are required to further assess the viability of this counterpart.

4.3 Non-thermal Emission

As of this writing, the non-thermal emission from GW170817 still displays a single synchrotron power-law spectral energy distribution extending from the X-rays to the radio band, and a luminosity that has reached a peak and is now decreasing (Alexander et al. 2018; Nyoka et al. 2018). Models that can account for this behavior include an off-axis jet with an angle-dependent Lorentz factor (a ‘structured jet’) or a quasi-spherical blast wave with radial structure.

The fastest ejecta in our GRMHD model has too much kinetic energy relative to models that can fit the observations of GW170817 (§3.4.2). Our initial magnetic field is poloidal in shape and strong in magnitude ($\sim 4 \times 10^{14}$ G), which optimizes the conditions for the emergence of a relativistic outflow. Use of other initial

conditions, including a weaker field with a significant toroidal component, will likely result in a weaker jet and lower kinetic power output.

5 SUMMARY AND OUTLOOK

We have performed long-term, 3D GRMHD simulations of BH accretion disks formed during neutron star mergers. Our models start with an equilibrium torus, a strong poloidal field, and make use of a suitably calibrated gamma-law equation of state, with approximations for the temperature, neutrino cooling, and nuclear recombination that account for the dominant effects of realistic microphysics on the dynamics and composition of the flow. These approximations enable us to maximize the amount of physical time simulated and therefore achieve completion of mass ejection to large radii. To connect with previous work and to better diagnose the GRMHD results, we have also carried out 2D hydrodynamic simulations with shear viscosity and a pseudo-Newtonian potential, and identical treatment of other physics. Our main results are the following:

1. – When including MHD effects in general relativity, the total mass ejected from the disk is 40% of the initial torus mass ($0.013 M_\odot$ for an initial torus mass of $0.033 M_\odot$; Table 1 and Figure 9). This is larger by a factor of two relative to hydrodynamic models.

2. – The ejected mass in the GRMHD model displays a broad distribution of electron fraction, entropy, and radial velocity (Figure 10). The majority of the outflow has $Y_e < 0.25$ and will thus result in a lanthanide-rich composition. When scaling our ejected fractions to a disk mass of $0.1 M_\odot$, the outflow from the GRMHD model can easily account for the (nominal) mass and velocity of the red kilonova from GW170817. The disk does not eject sufficient material with $Y_e > 0.25$ to account for the blue kilonova, however, despite achieving the right velocity ($0.22c$, Table 1). We caution, however, that our treatment of weak interactions is approximate and does not include neutrino absorption. Also, the composition of the early outflow will depend more sensitively on the initial distribution of Y_e produced during the merger, which may be on average higher than the uniform and low value we assume (0.1). Finally, the appearance of the kilonova can depend on the details of the spatial distribution of the lanthanide mass fraction (e.g., Kasen et al. 2017), which in turn depends on the degree of mixing and/or stratification of the electron fraction, not just on the bulk amounts above or below $Y_e \sim 0.25$.

3. – Mass ejection in MHD can be divided into two phases: an early ($t \leq 1$ s as measured from $r = 10^9$ cm), magnetically-mediated phase, absent in hydrodynamic models, and a late phase following freezeout of weak interactions (Figures 3 and 6), which operates on the angular-momentum transport timescale. The slow component ($v^r/c < 0.1$) of the late-time outflow shows similar properties in both MHD and in hydrodynamic models (Figure 14). This similarity points to a shared mechanism for mass ejection: neutrino cooling freezes out and thermal energy is deposited by turbulent dissipation or viscous heating, and by recombination of nucleons into alpha particles. The GRMHD model has an additional fast component at late times which must be mediated by magnetic processes given its absence in hydrodynamic models. The accretion history, late-time mass ejection, and neutrino luminosity of the GRMHD model is

bracketed by the hydrodynamic models that use $\alpha = 0.03$ and $\alpha = 0.1$ (Figures 6, 7, and 9).

4. – Given our initial field geometry, which is optimized for efficient extraction of energy from the BH, we obtain a robust jet carrying 3×10^{50} erg of electromagnetic energy (in all directions; Figure 8). A small fraction of the ejecta achieves relativistic velocities at latitudes close to the rotation axis (Figure 12 and 13). Comparing with models that fit the non-thermal emission from GW170817 shows that our model contains too much kinetic energy in matter with $\gamma\beta \gtrsim 1$ (§3.4.2). The angular dependence of our jet is compatible with off-axis fits to the non-thermal emission from GW170817 (Figure 13). We caution that this component of the disk outflow will almost certainly interact with the dynamical ejecta, and thus the final kinetic energy distribution in a realistic setting will likely differ from that in our models.

5. – A few percent of the ejecta in the GRMHD model ($7 \times 10^{-4} M_{\odot}$) also has sufficient velocity and low Y_e to generate free neutrons not captured onto nuclei during the r -process (§4). This component can generate early (\sim hr timescale) thermal emission preceding the kilonova. The existence of this component is likely to also be sensitive to the initial magnetic field configuration, and on its location relative to the dynamical ejecta.

Our GRMHD model can be improved in many ways to achieve a more realistic result. The simplest modification is changing the initial field geometry, which is bound to have the largest impact on the fastest portion of the ejecta. We have adopted a strong poloidal field with a topology that maximizes energy extraction from the BH. A more realistic disk is expected to contain a significant toroidal component (e.g., Etienne et al. 2012; Kiuchi et al. 2014) that can be highly turbulent from the time of disk formation (and thus generate a different thermal evolution than our equilibrium initial conditions).

A more challenging improvement involves a realistic treatment of neutrinos (emission and absorption) and microphysics (EOS with full nuclear recombination). For the case of a promptly-formed BH, the effect of neutrino absorption on the bulk of the outflow dynamics is likely to be secondary, given that (1) in hydrodynamic models, for which the outflow is slow and similar to the slow MHD component at late times, absorption is unimportant, and (2) inclusion of magnetic fields adds a fast component which neutrinos have a smaller chance to modify given its rapid expansion. Nevertheless, neutrino absorption is crucial for determining a reliable composition and therefore detailed r -process yields for comparison with observations (as demonstrated by Siegel & Metzger 2018 who assess the effect of neutrino absorption in post-processing). Also, in the case of weak magnetic fields, neutrino energy deposition can combine with magnetic stresses in launching a successful jet (e.g., Just et al. 2016; Perego et al. 2017), and the magnitude of this energy deposition is very sensitive to the neutrino scheme adopted (Foucart et al. 2018). If a HMNS survives for longer than a dynamical time, the effect of neutrinos become dynamically important and proper neutrino transport is essential for a complete description.

Finally, more realistic initial conditions for density, temperature, and electron fraction can be obtained by mapping from a dynamical merger simulation (as in Nouri et al. 2017). While the details of the initial thermodynamics and composition have a relatively minor ($\sim 10\%$) effect on the late-time slow disk outflow composition (Fernández et al. 2017), the prompt MHD outflow preserves the initial composition of the disk. Also, the mapping from

binary parameters (total mass, mass ratio, spins, etc.) to initial disk mass and field geometry is non-trivial and essential for detailed comparison with observations. Finally, evaluating the feasibility of models that rely on the interaction of a jet with the dynamical ejecta (such as models involving cocoon emission; e.g. Nagakura et al. 2014; Lazzati et al. 2017; Gottlieb et al. 2018) requires proper initial conditions for all merger remnant components.

ACKNOWLEDGMENTS

We thank Meng-Ru Wu, Yong-Zhong Qian, and Stéphane Goriely for helpful discussions. We also thank Daniel Siegel for providing additional information about published simulation results, and Austin Harris for help with running simulations. The anonymous referee provided constructive comments that improved the presentation of the paper. RF acknowledges support from the Natural Sciences and Engineering Research Council (NSERC) of Canada, and from the Faculty of Science at the University of Alberta. AT acknowledges support from Northwestern University. EQ was supported in part by a Simons Investigator award from the Simons Foundation, and the David and Lucile Packard Foundation. This work was also supported in part by the Gordon and Betty Moore Foundation through Grant GBMF5076. Support for this work was provided by NASA through Einstein Postdoctoral Fellowship grant numbered PF4-150122 (FF) and PF3-140115 (AT) awarded by the Chandra X-ray Center, which is operated by the Smithsonian Astrophysical Observatory for NASA under contract NAS8-03060, and through grant 80NSSC18K0565 (FF, AT). DK is supported by the U.S. Department of Energy, Office of Science, Office of Nuclear Physics, under contract numbers DE-AC02-05CH11231, de-sc0017616, and de-sc0018297. The software used in this work was in part developed by the DOE NNSA-ASC OASCR Flash Center at the University of Chicago. This research used resources of the National Energy Research Scientific Computing Center (NERSC), which is supported by the Office of Science of the U.S. Department of Energy under Contract No. DE-AC02-05CH11231. Computations were performed at Carver and Edison (repositories m1186, m2058, m2401, and the scavenger queue).

APPENDIX A: MICROPHYSICS APPROXIMATIONS

A1 Adiabatic Index

Here we compare the results from disk wind simulations using a physical EOS and a γ -law EOS, to choose the appropriate value of the adiabatic index for HARMPI GRMHD models and their hydrodynamic counterparts.

As a baseline of comparison, we take a representative disk model of F15, which includes the EOS of Timmes & Swesty (2000) with the abundances of neutrons, protons, and alpha particles in NSE. We focus on model s-a80, which has an initial disk mass $M_{i0} = 0.03 M_{\odot}$, a central BH with mass $M_{\text{bh}} = 3 M_{\odot}$ and spin $a = 0.8$, uses a viscosity parameter $\alpha = 0.03$, and employs optically thin neutrino source terms with optical depth corrections of the form $e^{-\tau}$, with τ an approximate optical depth. In addition to the fiducial model s-a80, we evolve three variants that remove key physics: one without nuclear recombination (s-a80-na), one without neutrino self-irradiation (s-a80-ni), and one without both nuclear recombination and neutrino self-irradiation (s-a80-na-ni). The grid is similar to that described in §2.3, but with a resolution of 56 cells in the polar direction and 64 cells per decade in radius,

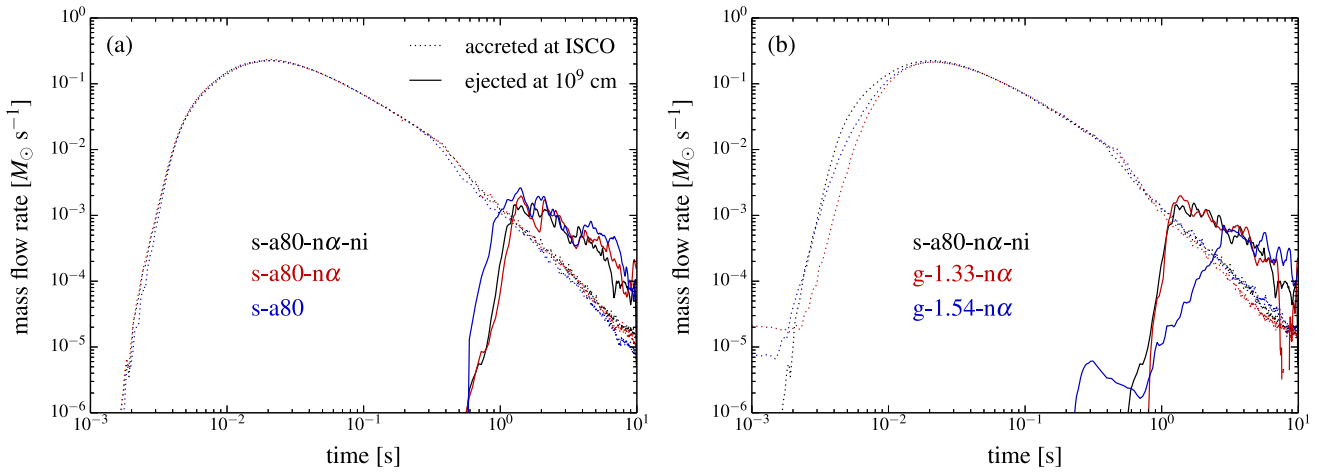


Figure A1. Comparison of mass outflow and accretion in models with physical and γ -law EOSs. Shown is the mass accretion rate at the ISCO (dotted lines) and outflow rates at 10^9 cm (solid lines) for selected models from Table A1. Panel (a) shows the effect of removing key physics from the s-a80 series of models, while panel (b) compares the γ -law models with the physical model with no α particle recombination or neutrino self-irradiation. The best agreement in mass ejection is obtained with $\gamma_{\text{ad}} = 4/3$.

with an effective cell size $\Delta r/r \simeq \Delta \theta \simeq 2^\circ$ at the equator (lower in each direction by a factor two relative to the hydrodynamic models in Table 1).

We evolve 3 comparison γ -law models at the same resolution, using the physics described in §2.1. Two models exclude nuclear recombination, one of them using the adiabatic index at the initial density maximum in model s-a80 ($\gamma_{\text{ad}} = 1.54$, model g-1.54- $n\alpha$), and the other using the adiabatic index in the wind at late times ($\gamma_{\text{ad}} = 4/3$, model g-1.33- $n\alpha$). A third model includes nuclear recombination as described in §2.1 using $\gamma_{\text{ad}} = 4/3$, and is thus a lower resolution version of model h2d-v03 from Table 1.

Table A1 shows the mass ejection properties for the comparison models, with selected cases shown in Figure A1. The exclusion of nuclear recombination in the models with a physical EOS causes a $\sim 30\%$ reduction in the total mass ejection, whereas excluding self-irradiation hardly changes the result. Excellent agreement is found between models s-a80- $n\alpha$ -ni and g-1.33- $n\alpha$ in the integrated and instantaneous mass ejection. In contrast, the model with $\gamma_{\text{ad}} = 1.54$ ejects a much smaller amount of mass (30% less than the model with $\gamma_{\text{ad}} = 4/3$). On the other hand, the accretion history at the ISCO is most similar for models s-a80- $n\alpha$ -ni and g-1.54- $n\alpha$. Given that this study focuses on the late-time wind properties, we adopt $\gamma_{\text{ad}} = 4/3$ as the adiabatic index of our fiducial production models.

The contribution from alpha particle recombination is stronger in model g-1.33 than in s-a80-ni. Note however that doubling the resolution in angle and radius can also lead to differences in mass ejection of the order of $\sim 10\%$, so we consider agreement between these two models to be acceptable.

A2 Degeneracy

While the effects of electron degeneracy on the total pressure are not dominant, its inclusion in the neutrino rates is crucial for obtaining an adequate level of neutron richness. In particular, degeneracy strongly suppresses the positron density, because pairs are created in the exponential tail of the thermal distribution above the Fermi sphere (e.g., Beloborodov 2003). The lack of positron captures leads to an overabundance of neutrons.

Table A1. Comparison models and mass ejection properties. Columns from left to right show model name, type of EOS (helm: physical, γ_{ad} : gamma-law), inclusion of α particle recombination energy, inclusion of neutrino self-irradiation, total mass ejection in units of the initial torus mass, and time- and mass-flux-averaged \bar{Y}_e in the wind.

Model	EOS	α	Irr.	$M_{\text{ej}}/M_{\text{t0}}$	\bar{Y}_e
s-a80	helm	Y	Y	0.18	0.22
s-a80-ni			N	0.18	0.22
s-a80- $n\alpha$		N	Y	0.13	0.23
s-a80- $n\alpha$ -ni			N	0.12	0.23
g-1.33	$\gamma_{\text{ad}} = 4/3$	Y	N	0.20	0.21
g-1.33- $n\alpha$		N		0.12	0.22
g-1.54- $n\alpha$	$\gamma_{\text{ad}} = 1.54$			0.09	0.20

We compute the level of electron degeneracy analytically in the relativistic limit ($kT \gg m_e c^2 \simeq 0.5$ MeV). We start by writing the net electron density in terms of the degeneracy parameter (e.g., Bethe et al. 1980):

$$n_{e^-} - n_{e^+} = \frac{1}{\pi^2} \left(\frac{kT}{\hbar c} \right)^3 [\mathcal{F}_2(\eta_e) - \mathcal{F}_2(-\eta_e)] \quad (\text{A1})$$

$$= \frac{1}{3\pi^2} \left(\frac{kT}{\hbar c} \right)^3 [\pi^2 \eta_e + \eta_e^3] \quad (\text{A2})$$

where $\eta_e = \mu_e/(kT)$ is the chemical potential of electrons. Writing $n_{e^-} - n_{e^+} = \rho Y_e/m_n$ and using the Fermi momentum $p_F = \hbar(3\pi^2 Y_e \rho/m_n)^{1/3}$, we obtain a cubic equation for η_e in terms of $\{\rho, T, Y_e\}$:

$$\eta_e^3 + \pi^2 \eta_e - \left(\frac{p_{\text{FC}}}{kT} \right)^3 = 0. \quad (\text{A3})$$

This equation has the solution

$$\eta_e = \left[\frac{1}{2} \left(\frac{p_{\text{FC}}}{kT} \right)^3 + \sqrt{\frac{1}{4} \left(\frac{p_{\text{FC}}}{kT} \right)^6 + \frac{\pi^6}{27}} \right]^{1/3} + \left[\frac{1}{2} \left(\frac{p_{\text{FC}}}{kT} \right)^3 - \sqrt{\frac{1}{4} \left(\frac{p_{\text{FC}}}{kT} \right)^6 + \frac{\pi^6}{27}} \right]^{1/3}, \quad (\text{A4})$$

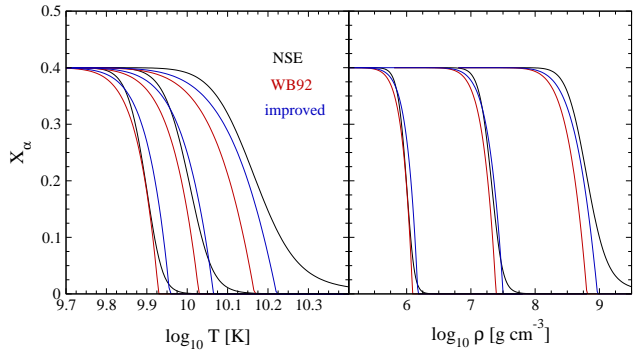


Figure A2. Comparison between the mass fractions of alpha particles obtained from an NSE calculation (black), the analytic fit of Woosley & Baron (1992) (red), and equation (13) (blue). The latter differs from Woosley & Baron (1992) by a global factor of $2^{-3/4}$ introduced to improve agreement in the thermodynamic regime of interest. The thermodynamic trajectories assume $T^3/\rho = \text{constant}$ and $Y_e = 0.2$.

with limiting cases

$$\eta_e \approx \begin{cases} \left(\frac{P_{\text{FC}}}{kT}\right) & P_{\text{FC}} \gg \pi kT \\ \frac{1}{\pi^2} \left(\frac{P_{\text{FC}}}{kT}\right)^3 & P_{\text{FC}} \ll \pi kT. \end{cases} \quad (\text{A5})$$

We set $\eta_e = 0$ for $T < 1$ MeV, for which neutrino source terms become sub-dominant.

To include the effects of degeneracy in the neutrino rates, we need to calculate individual Fermi functions for input in eqns. (6)-(7) and evaluate them with η_e obtained from eq. (A4). The Fermi functions of negative argument are obtained using a well-known series expansion (e.g., McDougall & Stoner 1938):

$$\mathcal{F}_4(-\eta) = 4! \left[e^{-\eta} - \frac{e^{-2\eta}}{2^5} + \frac{e^{-3\eta}}{3^5} - \dots \right] \quad (\text{A6})$$

$$\mathcal{F}_5(-\eta) = 5! \left[e^{-\eta} - \frac{e^{-2\eta}}{2^6} + \frac{e^{-3\eta}}{3^6} - \dots \right]. \quad (\text{A7})$$

We take the first three terms in the series, as in Shibata et al. (2007), yielding values that are accurate to better than 1% for $\eta = 0$. We then obtain the Fermi functions of positive argument using the exact relations between sums and differences from Bludman & van Riper (1978):

$$\mathcal{F}_4(\eta) - \mathcal{F}_4(-\eta) = \frac{7\pi^4}{15}\eta + \frac{2\pi^2}{3}\eta^3 + \frac{1}{5}\eta^5 \quad (\text{A8})$$

$$\mathcal{F}_5(\eta) + \mathcal{F}_5(-\eta) = \frac{31\pi^6}{126} + \frac{7\pi^4}{6}\eta^2 + \frac{5\pi^2}{6}\eta^4 + \frac{1}{6}\eta^6. \quad (\text{A9})$$

The comparison models shown in Table A1 indicate that including degeneracy in the rate of change of Y_e due to neutrino and antineutrino emission (equation 3) leads to average electron fractions that are very similar to those obtained when more physics is included (as in the s-a80-type models).

A3 Approximation to Nuclear Statistical Equilibrium

Figure A2 compares the results of an NSE calculation for the mass fraction of α particles (e.g., Shapiro & Teukolsky 1983) with the analytic fit of Woosley & Baron (1992). This fit has been used in a number of NS merger remnant disk studies to parameterize the effects of nuclear recombination (e.g., Popham et al. 1999; Di Matteo et al. 2002; Lee et al. 2005; Shibata et al. 2007). The curves

in Figure A2 keep T^3/ρ constant, as appropriate for wind particles in a medium dominated by radiation pressure and in which other energy source terms are unimportant, and assume $Y_e = 0.2$.

Figure A2 shows curves for three values of the entropy which span the relevant thermodynamic range spanned by the wind. The fit of Woosley & Baron (1992) systematically underestimates the characteristic densities and temperatures at the point where the transition from α -particles to pure nucleons takes place, with the error being larger at higher densities. Nonetheless, a minor adjustment to the numerical prefactor, from 26.2 to $15.6 \approx 26.2/2^{3/4}$, shifts the curves closer to the NSE results. Quantitatively, the fractional errors in the temperatures and densities at the point where $X_\alpha = Y_e = 0.2$ are {5, 3, 5}% and {16, 10, 13}%, for the low, medium, and high density trajectories, respectively.

REFERENCES

- Abbott B. P., et al., 2017a, *ApJ*, 850, L39
 Abbott B. P., et al., 2017b, *ApJ*, 848, L13
 Abbott B. P., et al., 2017c, *PRL*, 119, 161101
 Abbott B. P., et al., 2017d, *ApJ*, 848, L12
 Abbott B. P., et al., 2018, preprint, arXiv:1805.11581
 Alexander K. D., et al., 2018, preprint, arXiv:1805.02870
 Artemova I. V., Bjoernsson G., Novikov I. D., 1996, *ApJ*, 461, 565
 Balbus S. A., Hawley J. F., 1991, *ApJ*, 376, 214
 Barnes J., Kasen D., 2013, *ApJ*, 775, 18
 Bauswein A., Goriely S., Janka H.-T., 2013, *ApJ*, 773, 78
 Bauswein A., Just O., Janka H.-T., Stergioulas N., 2017, *ApJ*, 850, L34
 Beloborodov A. M., 2003, *ApJ*, 588, 931
 Beloborodov A. M., 2008, in Axelsson M., ed., *American Institute of Physics Conference Series Vol. 1054 of American Institute of Physics Conference Series, Hyper-accreting black holes*. pp 51–70
 Bernuzzi S., Dietrich T., Tichy W., Brüggmann B., 2014, *PRD*, 89, 104021
 Bethe H. A., Applegate J. H., Brown G. E., 1980, *ApJ*, 241, 343
 Bludman S. A., van Riper K. A., 1978, *ApJ*, 224, 631
 Bovard L., Martin D., Guercilena F., Arcones A., Rezzolla L., Korobkin O., 2017, *PRD*, 96, 124005
 Chatziioannou K., Haster C.-J., Zimmerman A., 2018, preprint, arXiv:1804.03221
 Chen W.-X., Beloborodov A. M., 2007, *ApJ*, 657, 383
 Chornock R., et al., 2017, *ApJ*, 848, L19
 Côté B., Fryer C. L., Belczynski K., Korobkin O., Chruślińska M., Vassh N., Mumpower M. R., Lippuner J., Sprouse T. M., Surman R., Wollaeger R., 2018, *ApJ*, 855, 99
 Cowling T. G., 1933, *MNRAS*, 94, 39
 Cowperthwaite P. S., et al., 2017, *ApJ*, 848, L17
 D’Avanzo P., et al., 2018, *A&A*, 613, L1
 De S., Finstad D., Lattimer J. M., Brown D. A., Berger E., Biwer C. M., 2018, preprint, arXiv:1804.08583
 De Villiers J.-P., Hawley J. F., Krolik J. H., Hirose S., 2005, *ApJ*, 620, 878
 Di Matteo T., Perna R., Narayan R., 2002, *ApJ*, 579, 706
 Drout M. R., et al., 2017, *Science*, 358, 1570
 Dubey A., Antypas K., Ganapathy M. K., Reid L. B., Riley K., Sheeler D., Siegel A., Weide K., 2009, *J. Par. Comp.*, 35, 512
 Endrizzi A., Ciolfi R., Giacomazzo B., Kastaun W., Kawamura T., 2016, *CQG*, 33, 164001

- Etienne Z. B., Liu Y. T., Paschalidis V., Shapiro S. L., 2012, PRD, 85, 064029
- Fernández R., Foucart F., Kasen D., Lippuner J., Desai D., Roberts L. F., 2017, CQG, 34, 154001
- Fernández R., Kasen D., Metzger B. D., Quataert E., 2015, MNRAS, 446, 750
- Fernández R., Metzger B. D., 2013a, MNRAS, 435, 502
- Fernández R., Metzger B. D., 2013b, ApJ, 763, 108
- Fernández R., Metzger B. D., 2016, ARNPS, 66, 23
- Fishbone L. G., Moncrief V., 1976, ApJ, 207, 962
- Fontes C. J., Fryer C. L., Hungerford A. L., Hakel P., Colgan J., Kilcrease D. P., Sherrill M. E., 2015, High Energy Density Physics, 16, 53
- Foucart F., Duez M. D., Kidder L. E., Nguyen R., Pfeiffer H. P., Scheel M. A., 2018, preprint, arXiv:1806.02349
- Foucart F., et al., 2015, PRD, 91, 124021
- Foucart F., et al., 2016, PRD, 93, 044019
- Foucart F., O'Connor E., Roberts L., Kidder L. E., Pfeiffer H. P., Scheel M. A., 2016, PRD, 94, 123016
- Fryxell B., Olson K., Ricker P., Timmes F. X., Zingale M., Lamb D. Q., MacNeice P., Rosner R., Truran J. W., Tufo H., 2000, ApJS, 131, 273
- Fujibayashi S., Kiuchi K., Nishimura N., Sekiguchi Y., Shibata M., 2018, ApJ, 860, 64
- Gammie C. F., McKinney J. C., Tóth G., 2003, ApJ, 589, 444
- Goriely S., Bauswein A., Janka H.-T., Sida J.-L., Lemaître J.-F., Panebianco S., Dubray N., Hilaire S., 2014, in Jeong S., Imai N., Miyatake H., Kajino T., eds, American Institute of Physics Conference Series Vol. 1594 of American Institute of Physics Conference Series, The r-process nucleosynthesis during the decompression of neutron star crust material. pp 357–364
- Gottlieb O., Nakar E., Piran T., 2018, MNRAS, 473, 576
- Guilet J., Bauswein A., Just O., Janka H.-T., 2017, MNRAS, 471, 1879
- Haggard D., Nynka M., Ruan J. J., Kalogera V., Cenko S. B., Evans P., Kennea J. A., 2017, ApJ, 848, L25
- Hawley J. F., 2000, ApJ, 528, 462
- Hawley J. F., Krolik J. H., 2006, ApJ, 641, 103
- Hotokezaka K., Beniamini P., Piran T., 2018, preprint, arXiv:1801.01141
- Hotokezaka K., Kiuchi K., Kyutoku K., Okawa H., Sekiguchi Y.-i., Shibata M., Taniguchi K., 2013, Phys. Rev. D, 87, 024001
- Hotokezaka K., Kiuchi K., Shibata M., Nakar E., Piran T., 2018, preprint, arXiv:1803.00599
- Janiuk A., 2017, ApJ, 837, 39
- Janiuk A., Mioduszewski P., Moscibrodzka M., 2013, ApJ, 776, 105
- Janka H.-T., 2001, A&A, 368, 527
- Just O., Bauswein A., Pulpillo R. A., Goriely S., Janka H.-T., 2015, MNRAS, 448, 541
- Just O., Obergaulinger M., Janka H.-T., Bauswein A., Schwarz N., 2016, ApJ, 816, L30
- Kasen D., Badnell N. R., Barnes J., 2013, ApJ, 774, 25
- Kasen D., Fernández R., Metzger B. D., 2015, MNRAS, 450, 1777
- Kasen D., Metzger B., Barnes J., Quataert E., Ramirez-Ruiz E., 2017, Nature, 551, 80
- Kastaun W., Galeazzi F., 2015, PRD, 91, 064027
- Kastaun W., Galeazzi F., Alic D., Rezzolla L., Font J. A., 2013, PRD, 88, 021501
- Kawaguchi K., Shibata M., Tanaka M., 2018, preprint, arXiv:1806.04088
- Kiuchi K., et al., 2015, Phys.Rev.D, 92, 064034
- Kiuchi K., Kyutoku K., Sekiguchi Y., Shibata M., Wada T., 2014, PRD, 90, 041502
- Kiuchi K., Kyutoku K., Shibata M., 2012, PRD, 86, 064008
- Lazzati D., Deich A., Morsony B. J., Workman J. C., 2017, MNRAS, 471, 1652
- Lazzati D., Perna R., Morsony B. J., Lopez-Camara D., Cantiello M., Ciolfi R., Giacomazzo B., Workman J. C., 2018, PRL, 120, 241103
- Lee W. H., Ramirez-Ruiz E., López-Cámara D., 2009, ApJ, 699, L93
- Lee W. H., Ramirez-Ruiz E., Page D., 2005, ApJ, 632, 421
- Lehner L., Pretorius F., 2014, ARA&A, 52, 661
- Li L.-X., Paczyński B., 1998, ApJ, 507, L59
- Lippuner J., Fernández R., Roberts L. F., Foucart F., Kasen D., Metzger B. D., Ott C. D., 2017, MNRAS, 472, 904
- Liska M. T. P., Tchekhovskoy A., Quataert E., 2018, preprint, arXiv:1809.04608
- Margalit B., Metzger B. D., 2017, ApJ, 850, L19
- Margutti R., et al., 2018, ApJ, 856, L18
- Martin D., Perego A., Arcones A., Thielemann F.-K., Korobkin O., Rosswog S., 2015, ApJ, 813, 2
- McDougall J., Stoner E. C., 1938, Royal Society of London Philosophical Transactions Series A, 237, 67
- McKinney J. C., Tchekhovskoy A., Blandford R. D., 2012, MNRAS, 423, 3083
- Metzger B. D., 2017, Living Reviews in Relativity, 20, 3
- Metzger B. D., Bauswein A., Goriely S., Kasen D., 2015, MNRAS, 446, 1115
- Metzger B. D., Fernández R., 2014, MNRAS, 441, 3444
- Metzger B. D., Martínez-Pinedo G., Darbha S., Quataert E., Arcones A., Kasen D., Thomas R., Nugent P., Panov I. V., Zinner N. T., 2010, MNRAS, 406, 2650
- Metzger B. D., Piro A. L., Quataert E., 2009, MNRAS, 396, 304
- Metzger B. D., Thompson T. A., Quataert E., 2018, ApJ, 856, 101
- Mooley K. P., et al., 2018, Nature, 554, 207
- Nagakura H., Hotokezaka K., Sekiguchi Y., Shibata M., Ioka K., 2014, ApJ, 784, L28
- Narayan R., Piran T., Kumar P., 2001, ApJ, 557, 949
- Narayan R., Sądowski A., Penna R. F., Kulkarni A. K., 2012, MNRAS, 426, 3241
- Narayan R., Yi I., 1994, ApJ, 428, L13
- Noble S. C., Gammie C. F., McKinney J. C., Del Zanna L., 2006, ApJ, 641, 626
- Nouri F. H., Duez M. D., Foucart F., Deaton M. B., Haas R., Haddadi M., Kidder L. E., Ott C. D., Pfeiffer H. P., Scheel M. A., Szilagy B., 2017, preprint, arXiv:1710.07423
- Nynka M., Ruan J. J., Haggard D., 2018, preprint, arXiv:1805.04093
- Paschalidis V., Ruiz M., Shapiro S. L., 2015, ApJ, 806, L14
- Perego A., Rosswog S., Cabezón R. M., Korobkin O., Käppeli R., Arcones A., Liebendörfer M., 2014, MNRAS, 443, 3134
- Perego A., Yasin H., Arcones A., 2017, Journal of Physics G Nuclear Physics, 44, 084007
- Popham R., Woosley S. E., Fryer C., 1999, ApJ, 518, 356
- Radice D., Galeazzi F., Lippuner J., Roberts L. F., Ott C. D., Rezzolla L., 2016, MNRAS, 460, 3255
- Raitel C. A., Özel F., Psaltis D., 2018, ApJ, 857, L23
- Rezzolla L., Giacomazzo B., Baiotti L., Granot J., Kouveliotou C., Aloy M. A., 2011, ApJ, 732, L6
- Rezzolla L., Most E. R., Weih L. R., 2018, ApJ, 852, L25
- Roberts L. F., Kasen D., Lee W. H., Ramirez-Ruiz E., 2011, ApJ,

736, L21

- Roberts L. F., Lippuner J., Duez M. D., Faber J. A., Foucart F., Lombardi Jr. J. C., Ning S., Ott C. D., Ponce M., 2017, *MNRAS*, 464, 3907
- Rosswog S., Sollerman J., Feindt U., Goobar A., Korobkin O., Fremling C., Kasliwal M., 2017, preprint, arXiv:1710.05445
- Ruffert M., Janka H.-T., 1999, *A&A*, 344, 573
- Ruiz M., Lang R. N., Paschalidis V., Shapiro S. L., 2016, *ApJ*, 824, L6
- Sądowski A., Narayan R., Penna R., Zhu Y., 2013, *MNRAS*, 436, 3856
- Sekiguchi Y., Kiuchi K., Kyutoku K., Shibata M., Taniguchi K., 2016, *PRD*, 93, 124046
- Shakura N. I., Sunyaev R. A., 1973, *A&A*, 24, 337
- Shapiro S. L., Teukolsky S. A., 1983, *Black holes, white dwarfs, and neutron stars: The physics of compact objects*. Wiley-Interscience, New York
- Shibata M., Fujibayashi S., Hotokezaka K., Kiuchi K., Kyutoku K., Sekiguchi Y., Tanaka M., 2017, *PRD*, 96, 123012
- Shibata M., Kiuchi K., Sekiguchi Y.-i., 2017, *PRD*, 95, 083005
- Shibata M., Sekiguchi Y., 2012, *Progress of Theoretical Physics*, 127, 535
- Shibata M., Sekiguchi Y.-i., Takahashi R., 2007, *Progress of Theoretical Physics*, 118, 257
- Shibata M., Taniguchi K., 2006, *PRD*, 73, 064027
- Siegel D. M., Ciolfi R., Rezzolla L., 2014, *ApJ*, 785, L6
- Siegel D. M., Metzger B. D., 2017, *Physical Review Letters*, 119, 231102
- Siegel D. M., Metzger B. D., 2018, *ApJ*, 858, 52
- Stone J. M., Pringle J. E., Begelman M. C., 1999, *MNRAS*, 310, 1002
- Tanaka M., 2016, *Advances in Astronomy*, 2016, 634197
- Tanaka M., et al., 2017, *PASJ*, 69, 102
- Tanaka M., Hotokezaka K., 2013, *ApJ*, 775, 113
- Tanvir N. R., et al., 2017, *ApJ*, 848, L27
- Tchekhovskoy A., Narayan R., McKinney J. C., 2011, *MNRAS*, 418, L79
- Timmes F. X., Swesty F. D., 2000, *ApJS*, 126, 501
- Tóth G., 2000, *Journal of Computational Physics*, 161, 605
- Wanajo S., Sekiguchi Y., Nishimura N., Kiuchi K., Kyutoku K., Shibata M., 2014, *ApJ*, 789, L39
- Woosley S. E., Baron E., 1992, *ApJ*, 391, 228
- Wu M.-R., Fernández R., Martínez-Pinedo G., Metzger B. D., 2016, *MNRAS*, 463, 2323